Effect of soil moisture during hydrological drought on peak flow: insights from data analysis and 3Di modelling

Case study in the Hupselse Beek

Anaís del Solar Schaap

Delft University of Technology

TU Delft

Nelen & Schuurmans

Effect of soil moisture during hydrological drought on peak flow: insights from data analysis and 3Di modelling

Case study in the Hupselse Beek

by

Anaís del Solar Schaap

to obtain the degree of Master of Science
at the Delft University of Technology,
to be defended publicly on Friday, October 10, 2025 at 14:00.

Student number:	4917413	
Project duration:	March 3, 2025 – October 10, 2025	
Thesis committee:	Dr. habil. M. Hrachowitz,	TU Delft, supervisor
	Dr. Ir. A.M.J. Coenders,	TU Delft
	E. van der Laan,	Nelen en Schuurmans
	M. Blom,	Nelen en Schuurmans

Cover: Photo of Hupselse Beek, taken by the author

An electronic version of this thesis is available at http://repository.tudelft.nl/.

TU Delft

Nelen & Schuurmans

Preface

Before you lies my MSc thesis report, the result of eight months of work. During the course of my thesis, global events such as the meteorological drought in the Netherlands during spring and the flood in Texas highlighted the relevance of my research in the context of climate change. I am glad I could contribute! Looking back, I realize how much I have learned: from critically analyzing data to mastering a new model and ultimately developing and applying it from scratch to a specific area. I am deeply grateful to all those who supported me along the way.

First of all, I would like to thank my supervisors. From TU Delft, Markus and Miriam provided valuable feedback that I can carry into future work. From Nelen & Schuurmans, Menno and Esther offered consistent guidance and support during our weekly meetings. I also appreciated the open atmosphere at the office, where colleagues were always willing to help. Special mention goes to Nici for the inloopuurtjes, Ruben for stepping in as substitute supervisor, Sjon for all the QGIS support, and Eefje for the early brainstorm that helped shape my research scope. Also at TU Delft, the students in the afstudeerhok made the experience a shared journey, with regular coffee breaks that helped us get through it together. Furthermore, I would like to thank Gerry from Waterschap Rijn & IJssel for providing valuable insights and data on the Hupsel, as well as arranging a site visit to the area.

Lastly, I am grateful to my family and friends for not only supporting me during my thesis, but also during my whole academic journey. To my parents: thank you for the support during every exam week, for helping me prep my presentations, and to all the rides during the weekend between home to Delft or Rotterdam (and also back and forth for my exchange in Lund). To my sisters: thanks for always making me laugh and creating the perfect distraction by watching tsitp during the summer. Thomas, thank you for putting up with my chaos and always listening me talk about my “peak performance” (as you would call it) research. Finally, to my friends, whether joining me in study sessions or in much-needed breaks, thank you for your support and the joy you brought along the way.

Enjoy reading!

Anaís del Solar Schaap
Delft, October 2025

Abstract

In the future, dry and wet extremes are projected to intensify, while the time between the extremes is expected to shorten. Therefore, both extremes should be analyzed and modelled together. Antecedent soil moisture strongly shapes catchment response: at low levels, more storage reduces run-off, but once a threshold is exceeded, run-off rises sharply in a non-linear way. Conversely, dry conditions may induce water repellency, leading to increased run-off even with low soil moisture levels. It remains unclear whether this non-linear relationship changes during drought–flood transitions, forming the first knowledge gap of this study. To address this, the study examines how soil moisture correlates with peak discharge during such transitions.

Furthermore, both hydrological and hydrodynamic studies have a modelling gap, as initial drought states are rarely included and modelling of compound extremes remains scarce. To address this, the 3Di hydrodynamic model is used, which has been widely applied for floods but not yet for droughts. This study examines how well 3Di simulates peak flow after drought using effective precipitation as input, and whether incorporating soil moisture conditions through recharge further improves the results.

The research is conducted in the Hupselse Beek as a case study. The standardized streamflow index (SSI) is a drought index that is used to assess the hydrological droughts. Criteria are set in order to find drought events, of which three are selected for further modelling within 3Di: one for calibration and two for validation. The correlation analysis is performed by analyzing run-off against the antecedent soil water content for all drought events.

In addition, a 3Di model of the study area is developed containing the domains of surface water and groundwater. Measurements are compared with model results to test performance. The simulations cover a one-week period that includes the extreme rainfall event. Horton infiltration values, effective porosity and hydraulic conductivity values are calibrated in a sequential way to see if the results can approach the observations, with performance assessed through key metrics.

The selected drought dataset contains 38 events, demonstrating a positive non-linear relationship between soil-water content and run-off. Furthermore, a threshold in soil water content is observed around 0.22 mm^3/mm^3. It is concluded that the Hupselse Beek remains responsive to soil moisture, even under hydrological drought conditions.

For 3Di, the groundwater results show relatively good key metric performance while the surface water deviates strongly in response to effective precipitation. For the recharge simulations, the results in performance are worse. The Horton infiltration needs to decrease to compensate for the decrease in input. The incorporation of soil moisture conditions, and the effect of not representing them therefore needs to be researched further for 3Di modelling. At the same time, the groundwater results highlight the potential of 3Di for modelling peak flows during hydrological drought.

Contents

List of Figures

List of Tables

Nomenclature

Abbreviations

Abbreviation	Definition
CDF	Cumulative distribution function
DEM	Digital elevation model
GEV	Generalized extreme value
GLEAM	Global Land Evaporation Amsterdam Model
GLG	Gemiddeld laagste grondwaterstand (Mean lowest groundwater level)
KGE	Kling–Gupta efficiency
logNSE	Log-transformed Nash–Sutcliffe efficiency
NSE	Nash–Sutcliffe efficiency
PBIAS	Percent bias
RMSE	Root mean square error
SMI	Standardized moisture index
SPI	Standardized precipitation index
SGI	Standardized groundwater index
SSI	Standardized streamflow index
SWC	Soil water content

Symbols

Symbol	Definition	Dimension
A	Catchment area	[L^2]
α	Variability ratio (used in KGE)	[$-$]
d	Day index (used in distribution functions)	[$-$]
E_A	Actual evaporation	[LT^{-1}]
E_I	Interception evaporation	[LT^{-1}]
E_P	Potential evaporation	[LT^{-1}]
E_T	Evapotranspiration	[LT^{-1}]
f_0	Initial infiltration capacity	[LT^{-1}]
f_{eq}	Equilibrium infiltration capacity	[LT^{-1}]
h_t^{obs}	Observed water level at time t	[L]
h_t^{sim}	Simulated water level at time t	[L]
$\overline{h}^{\text{obs}}$	Mean observed water level	[L]
$\overline{h}^{\text{sim}}$	Mean simulated water level	[L]
k	Infiltration decay constant	[T]
K	Hydraulic conductivity	[LT^{-1}]
$K_{\text{Strickler}}$	Strickler roughness coefficient, defined as $1/n$	[$L^{1/3}T^{-1}$]
L	Losses	[LT^{-1}]

Symbol	Definition	Dimension
n	Manning's roughness coefficient	$[TL^{-1/3}]$
N	Total number of time steps	$[-]$
P	Precipitation	$[LT^{-1}]$
P_E	Effective precipitation	$[LT^{-1}]$
p_t	Non-exceedance probability of discharge per unit area at time t	$[-]$
Q	Discharge	$[L^3T^{-1}]$
$Q_{30\text{day}}$	30-day rolling mean discharge	$[L^3T^{-1}]$
Q_i	Inflow discharge at boundary i	$[L^3T^{-1}]$
Q_k	Outflow discharge at boundary k	$[L^3T^{-1}]$
Q_t	Discharge at time t	$[L^3T^{-1}]$
R	Recharge, part of effective precipitation that cannot be stored in unsaturated zone	$[LT^{-1}]$
R_U	Part of effective precipitation that can be stored in unsaturated zone	$[LT^{-1}]$
S	Storage capacity	$[L]$
S_I	Interception storage capacity	$[L]$
$S_{I,\max}$	Maximum interception storage capacity	$[L]$
S_U	Unsaturated storage capacity	$[L]$
$S_{U,\max}$	Maximum unsaturated storage capacity	$[L]$
T	Transfer term, either sink or source	$[L^3T^{-1}]$
V	Storage volume of a computational cell	$[L^3]$
$F_d(x)$	Fitted cumulative distribution function for day d	$[-]$
γ	Bias ratio (used in KGE)	$[-]$
Φ^{-1}	Inverse of the standard normal cumulative distribution function	$[-]$
ϕ_{eff}	Effective porosity	$[-]$
r	Linear correlation coefficient	$[-]$
σ	Standard deviation	[same as variable]
β	Shape parameter controlling the relation between S_U and $S_{U,\max}$	$[-]$

1

Introduction

Droughts are one of the most significant climate change hazards, with severe consequences for affected populations, economies, and ecosystems (Pizzorni, Innocenti, and Tollin, 2024). As climate change progresses, extremes are expected to become more frequent and severe (IPCC, 2023). Over the last 30 years, observations show an increase in frequency of dry-to-wet transitions in some areas. Furthermore, studies indicate that the time between consecutive dry and wet extremes is decreasing, leading to shorter recovery times from drought impacts (Barendrecht et al., 2024). This suggests that regions experience quicker transitions from drought to heavy rainfall. Studies have also shown that because of the dry-to-wet transitions, effects after intense rainfall can either be reduced because of an observed lower streamflow response (Matanó et al., 2025), or amplified because of an observed increase in run-off driven by water repellency (Bodí et al., 2013; Lucas-Borja et al., 2019). In order to manage these effects, it is crucial to analyze the impact of drought on hydrological processes and how these shape the response to subsequent extreme rainfall. Considering droughts and floods together is key for developing effective management strategies, which in turn minimize negative societal and economic impacts (Brunner et al., 2021).

There are different types of droughts, where each type defines a specific stage within drought propagation. These types are characterized as meteorological, soil moisture (or agricultural), and hydrological droughts. Meteorological drought refers to a prolonged period of precipitation deficiency. Agricultural drought arises when soil moisture supply needed for vegetation is reduced. Lastly, hydrological drought refers to surface and subsurface water level anomalies. Together, these types reflect how drought propagates through the hydrological cycle: starting with a lack of rainfall, progressing to reduced soil moisture, and eventually leading to diminished groundwater supplies. In regions where water systems react quickly to changes, droughts are primarily caused by insufficient rainfall and tend to happen more frequently, although they are shorter in duration. Conversely, in systems that respond slowly, droughts resemble groundwater droughts, occurring less often but lasting longer (Van Loon, 2013).

To evaluate drought severity, standardized indices are often used, such as the standardized precipitation index (SPI) for measuring precipitation shortages, the standardized groundwater index (SGI) for assessing groundwater depletion, and the standardized streamflow index (SSI) for analyzing discharge droughts (Van Loon, 2015). The relationship between drought duration and severity depends on how drought conditions propagate through the hydrological system and on the interaction between climate and local water storage (Van Loon et al., 2016).

This study focuses on hydrological drought, the most severe stage, when surface water and groundwater levels are low. Analyzing this stage makes it possible to capture the strongest dry-to-wet transitions, from low streamflow and depleted soil moisture to peak flow induced by extreme rainfall. The SSI is therefore used to characterize hydrological drought events.

Soil moisture plays a crucial role in the development and persistence of droughts. During hydrological drought, soil moisture levels are generally low, as the drought has already surpassed soil moisture drought. Prolonged periods of low soil moisture can stress vegetation, disrupt ecosystem functionality, and reduce agricultural productivity (Berg and Sheffield, 2018). In this research, soil moisture is not used as a drought indicator, but rather to understand how conditions influence the transition from dry-to-wet extremes during hydrological drought. Streamflow is therefore adopted as indicator to characterize hydrological droughts.

Antecedent soil moisture conditions refer to the level of soil saturation before a precipitation event (Schoener and Stone, 2019). These conditions strongly influence the generation of run-off. Therefore, soil moisture is not only linked to drought, but also a key factor in catchment response to wet extremes. Observations show that there is a non-linear relationship between soil moisture and run-off, where an abrupt increase in streamflow occurs once a specific threshold of soil moisture is reached (Farrick and Branfireun, 2014). Many floods in Europe have been caused not only by intense rainfall, but also by already highly saturated soils (Ye et al., 2023). However, when soils become extremely dry, they can turn hydrophobic, increasing run-off. In semi-arid Mediterranean areas, soils have been observed to develop water repellency, decreasing infiltration rates and thereby increasing run-off (Bodí et al., 2013; Lucas-Borja et al., 2019). Furthermore, Lucas-Borja et al. (2019) found that land use influences soil water repellency in Mediterranean areas: high repellency was observed in forested areas, while low repellency was found in intensively cultivated land. In the Netherlands, soil water repellency has also been observed in grass-covered clayey peat and peaty clay soils, which are not only difficult to wet after drought but also particularly drought-prone (Dekker and Ritsema, 1996). The impact of antecedent soil moisture conditions on run-off thus depends on climate, region, land use, and soil type.

1.1. Knowledge gaps

An example where a dry-to-wet extreme occurred is in the Hupselse Beek, a small catchment in the east of the Netherlands. In August 2010, the Hupsel experienced an extreme rainfall event, with 160 mm of rain falling in just 24 hours. Since 1969, the discharge has exceeded 1000 l/s only six times, and 2010 was one of these instances. Although the 2010 event experienced 3.6 times more rainfall than the other events, it resulted in only a 2.2 times higher peak discharge, limiting the flood impacts. This was attributed to the dry conditions prior to the extreme rain event, as seen in the initial discharge which was 50 times lower than the other events (Brauer et al., 2018). This event highlights how antecedent drought conditions can modulate flood impacts. More analyses of peak flows following droughts are needed in order to better understand the transition from dry-to-wet extremes, with particular attention to antecedent soil moisture as a key hydrological factor.

Due to the development of more frequent and severe extremes, as well as faster transition from dry to wet extremes, it is crucial to consider droughts and peak flows as part of a unified hydrological perspective. Within previous literature, there is an increase in focus on atmospheric processes that drive the transition of the two extremes. They have been associated with atmospheric rivers, large-scale ocean-atmosphere processes and drought-enhanced rain production. However, literature lacks on hydrological processes that play a role within the transition, and whether they intensify or dampen effects following the extremes (Barendrecht et al., 2024). The study of Pizzorni et. al (2024) supports this, as it states that there is limited research on the interactions between floods and droughts. The impact of droughts on floods, and the hydrological processes that play a role forms the first knowledge gap in this research.

Another knowledge gap lies within the field of hydrodynamic and hydrological modelling related to peak flow after drought events. While hydrological extremes are already difficult to simulate, representing post-drought peak flows is particularly challenging (Muñoz-Castro et al., 2025). Although the recent study by Muñoz-Castro et al. (2025) evaluates compound extremes within hydrological modelling, such studies remain scarce. Also within hydrodynamic modelling, there are limited studies that explicitly account for initial drought states. Using an integrated model with varying antecedent soil conditions, the study of Saksena, Merwade, and Singhofen (2019) demonstrated that the driest scenario produced the lowest streamflow. This finding shows that flood simulations neglecting soil moisture can misrepresent flooding effects. Addressing this gap therefore requires modelling approaches that account for antecedent soil moisture conditions.

1.2. Research goal and questions

This research aims to investigate how soil moisture influences peak flow during hydrological drought. This addresses the limited knowledge on the transition of dry to wet transitions by identifying soil moisture as a key hydrological factor.

Moreover, the knowledge gap within modelling peak flow after drought events is addressed by modelling in the hydrodynamic software 3Di. This state-of-the-art hydrodynamic software was developed by a consortium including Nelen & Schuurmans, Deltares, TU Delft, and Stelling Hydraulics. 3Di can integrate overland flow, channel flow, groundwater and urban drainage (Nelen & Schuurmans, n.d.). While 3Di has primarily been used for flood modelling, it has not yet been applied for modelling drought. This study explores its potential for modelling peak flows following drought by incorporating dry antecedent moisture conditions through a hydrological bucket model. The research is conducted in collaboration with Nelen & Schuurmans.

The following research questions are formulated:

1. How do antecedent soil moisture conditions during a hydrological drought correlate with peak discharge during subsequent extreme rainfall events?

2. How does 3Di perform in simulating peak flow events after drought conditions when using effective precipitation as input?

3. How does incorporating soil moisture conditions through the unsaturated zone affect the simulation of peak discharge event after hydrological drought in the 3Di model?

In order to answer the research questions, this study acts as a case study and focuses on the Hupselse Beek, the brook which was struck by the extreme event in 2010.

2

Theoretical background 3Di

In order to understand the computations of 3Di, this chapter outlines the key processes and concepts involved. The information is based on the documentation of 3Di along with personal communication at Nelen & Schuurmans. First, the basic physical computations are described in Section 2.1 with a focus on groundwater in Subsection 2.1.1. Thereafter, Section 2.2 describes the subgrid technique, a method used for including terrain details inside model cells. This is followed by Section 2.3, which addresses the 1D domain with computational grid. Lastly, Section 2.4 explains the modelling workflow.

2.1. Physics used in computations

In 3Di, the computational domain is represented by a grid of 2D cells. The surface water layer is always included, while an additional groundwater layer can optionally be added. The groundwater layer is identical to the surface water layer and vertically linked to it. In this study, the groundwater layer is included. The flow in each domain is governed by the principle of mass balance. Through integrating over a control volume and discretization through space, the following equation is formed:

$$\frac{\partial V}{\partial t} = \sum_{\text{in},\, i} Q_i - \sum_{\text{out},\, k} Q_k + \sum_j T_j \tag{2.1}$$

where V represents the storage volume of a computational cell [L^3], Q_i^{in} the inflow discharge at boundary i [L^3T^{-1}], Q_k^{out} the outflow discharge at boundary k [L^3T^{-1}], and T_j a source or sink term (transfer) [L^3T^{-1}] to represent processes such as evaporation or seepage. The model uses a staggered grid: water levels and volumes are calculated at the cell centres, while velocities and discharges are calculated at the cell edges. Surface water fluxes are computed with the Saint-Venant equations, a depth-averaged form of the Navier–Stokes equations that describe horizontal variations in water depth under shallow-water conditions. Groundwater fluxes are described by Darcy's law, where the Dupuit approximation allows the flow to be simplified as horizontal flow (Nelen & Schuurmans (2025); R. van Zee & M. Blom, personal communication, February 2025).

The two 3Di domains are highlighted in Figure 2.1 by illustrating one computational cell for each domain. The mass balance equation is also included (Equation 2.1), with colour-coded components matching the arrows indicating flow. The domains are linked together through infiltration and exfiltration. Infiltration occurs when surface water enters the subsurface through a wet surface cell, while exfiltration begins when the groundwater level rises above the lowest bed level of the overlying surface water cell, allowing water to flow back to the surface. The vertical arrows representing these infiltration and exfiltration fluxes are circled and highlighted in yellow.

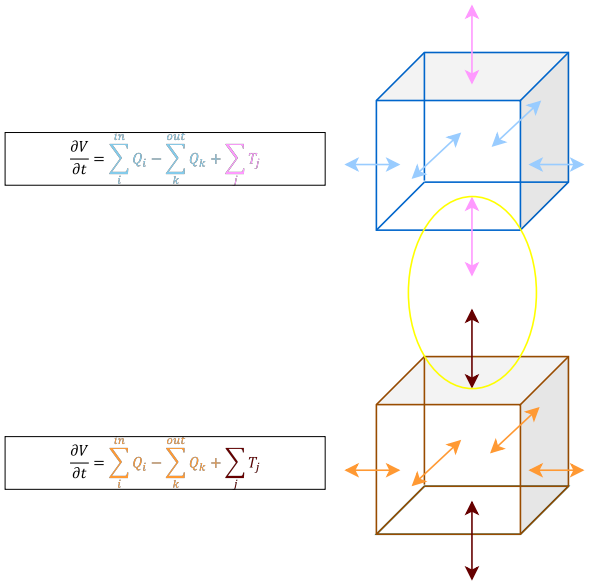

Figure 2.1: 3Di computational cells: upper for surface water elevation domain and lower for groundwater domain with included conservation of volume equation (Equation 2.1). Figure inspired from figure of 3Di training (Volp, 2025).

2.1.1. Groundwater

When adding the groundwater domain, settings need to be specified in order to define the groundwater flow. As stated in Section 2.1, exchange between the two domains is governed by infiltration or exfiltration. Infiltration is governed by Horton's equation, which models the infiltration rate as an exponentially decreasing function of time. Furthermore, it is assumed that the phreatic surface is equal to groundwater level, so everything above the groundwater table is dry. Effective porosity determines storage, while hydraulic conductivity governs horizontal groundwater flow, with both defined in the model settings. The bottom of the groundwater level is defined by the impervious layer level (Nelen & Schuurmans (2025); N. Volp, personal communication, April 2025). The detailed settings and initial values used in this study are described in Subsection 4.3.1.

2.2. Subgrid and grid refinement

Subgrid technique comes from the idea to balance computational cost and accuracy (Volp, Prooijen, and Stelling, 2013). The assumption is that water levels vary much more gradually than bathymetry. This leads to bathymetry to vary in a cell while the water level stays constant in a cell. Through this approach, 3Di has a high resolution subgrid, which contains detailed spatial information such as bathymetry and roughness, alongside a coarse computational grid where computations in the grid cells are performed. This way, high resolution information that can be included through rasters is taken into account in coarse grid computations. For the areas where detail is important, grid refinement is applied so that there is less loss in accuracy. This is done through the quad-tree refinement, a method where spatial refinement is achieved by splitting neighbouring cells into four, allowing multiple computational cell sizes within one grid. The minimum cell size is specified in the settings. Furthermore, when using the groundwater domain, the same same refinement is applied (Nelen & Schuurmans (2025); R. van Zee & M. Blom, personal communication, February 2025).

As described in Nelen & Schuurmans (2025), the following implications apply for the subgrid method:

- Storage capacity of domains is independent of grid size.
- Wet surface area changes with water level. When a cell is partially wet, the water level-volume relationship is non-linear.
- Automatic flooding and drying occur as a consequence of the non-linear water level-storage relationship. When a cell is only partially wet, this relationship is non-linear, whereas in a completely wet cell it becomes linear.

Figure 2.2a illustrates a computational cell with uniform water level and subgrid based bathymetry, indicated by orange blocks. The cell is partially wet since the water level has not yet exceeded the highest elevation. This highlights the non-linear relationship between water level and the volume. In addition, Figure 2.2b depicts a 2D raster of computational cells. Grid refinement is applied, which can be seen at the upper right corner of the figure. The water levels that are defined at the centre of the cells are illustrated with dots, while the velocities defined at the edges are illustrated with bars. These two representations are further distinguished by colour: the water level domain is shown in blue, and the momentum domains in green and orange.

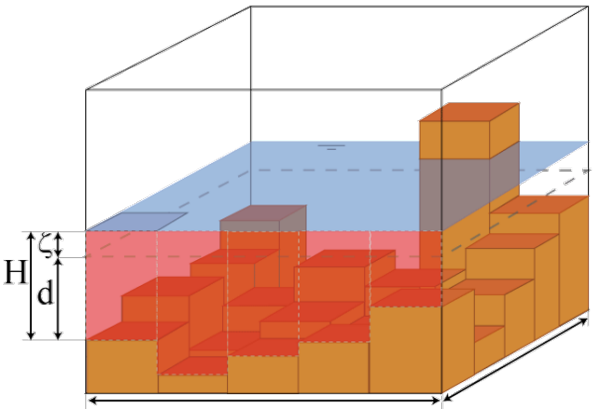

(a) Example of a computational cell with bathymetry based on subgrid.

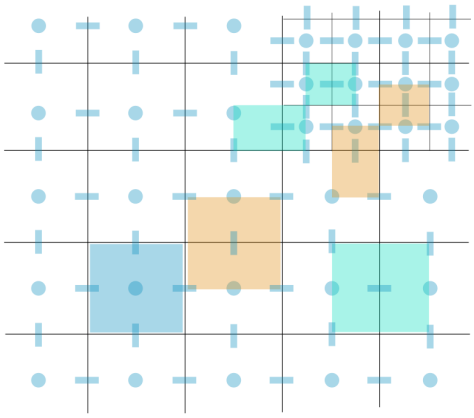

(b) Example of raster of computational cells with grid refinement. Water levels are defined at the centre of the cells (blue dots), while the velocities are defined at the edges (blue bars). Water level domain is shown in blue, and the momentum domains in green and orange.

Figure 2.2: Subgrid and grid refinement, illustrations from 3Di documentation (Nelen & Schuurmans, 2025).

2.3. 1D domain with computational grid

Next to the 2D domain of 3Di, there is also a 1D domain. This can consist of networks like channels or hydraulic structures like weirs, orifices, culverts and pipes. Like with the 2D domain, the 1D computational grid is also a staggered grid. In calculation nodes, water volumes are calculated and at the center of flowlines, velocities and discharges are calculated. Connection between the 1D and 2D domains is established by linking each 1D node to the closest cell center within the 2D computational grid through a 1D2D connection type (Nelen & Schuurmans (2025); R. van Zee & M. Blom, personal communication, February 2025).

2.4. Schematizations, models and simulations

The 3Di modelling process follows a structured workflow consisting of schematization, model setup, and simulation. A schematization contains information on rasters, vectors and settings. For instance, elevation is raster-based and 1D channel network or hydraulic structures such as weirs are vector-based. Settings define information on grid size, refinements or 1D2D connection types. From this schematization, a 3Di model is constructed, which in turn generates the computational grid used for calculations. A simulation is then created by adding a simulation template to the model. This template specifies initial conditions, boundary conditions and forcings (Nelen & Schuurmans (2025); R. van Zee & M. Blom, personal communication, February 2025).

3

Research area and data

As stated in Chapter 1, the Hupselse Beek forms the research area for this case study. This chapter maps the research area and describes its physical characteristics in Section 3.1. Furthermore, Section 3.2 describes the available meteorological and hydrological data, and argues what data is utilised for this research. Also, the validity of the data is tested to see if the data is feasible for drought analysis.

3.1. Research area

The Hupselse Beek is a rural lowland catchment area situated in the east of The Netherlands, between the towns of Eibergen and Groenlo near the German border. The area is chosen as it contains extensive data for drought analysis. Furthermore, it is a delineated brook with a relatively small area, allowing for robust results. Since the mid-1960's, the area has been a study area for hydrologists and students. The brook is the headwater of the 52 km² Leerinkbeek catchment area (Brauer et al., 2018). The area of the Hupsel catchment is 6.97 km² large, determined in QGIS based on data of layers provided by Waterschap Rijn & Ijssel. A map of the catchment area and its surroundings is shown in Figure 3.1. The colored points represent measurement points, further elaborated in Section 3.2.

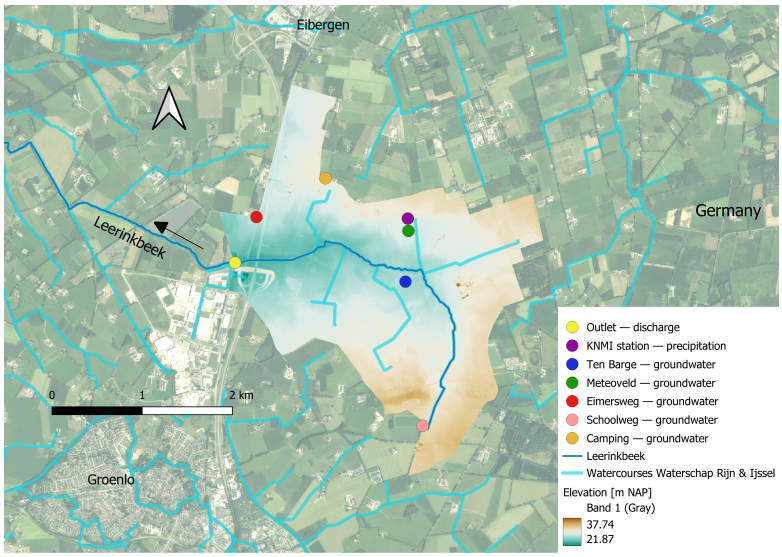

Figure 3.1: Illustration of research area outlined by elevation map with its surroundings. Aerial image obtained from the WMS service Actueel Ortho25 with a resolution of 25 cm is used to map the background. Water courses are illustrated with lines and measurement points with dots.

The land use mainly consists of grass, with some maize and a bit of forest, built up and surface water. Elevations range from 22 to 35 m above sea level, with the brook extending approximately 4 km and with a bed slope of 0.2%. The catchment is freely draining and the terrain slope is gentle (0.8%). Both the impermeable layer and the groundwater table are shallow (Brauer et al., 2018). Groundwater levels typically lie between between 0 to 0.5 m below soil surface during winter and 1.5 to 2.0 m depth during summer (Altayeb, 2023). Because of the shallow impermeable layer and the gentle terrain slope, the

area has been characterized as “flashy”, and in earlier times before drainage and retention measures it was prone to flooding (Brauer et al., 2018). This insinuates that the area reacts quickly to changes. Therefore, it is hypothesized that droughts in this area are short and happen on a frequent basis.

In addition, the soil consists of loamy sand and a bit of clay, peat and gravel. This layer varies in thickness from 0.2 m to 10 m across the area and lies on an impervious clay layer of more than 20 m thick. (Brauer et al., 2018). A vertical cross-section of the soil profile along the brook’s length is provided in Appendix B. The data is based from BRO REGIS II v2.2.3 and obtained via DinoLoket. In the study area, the shallow subsurface is composed of deposits from both the Formation of Boxtel (NUBx) and the Formation of Sterksel (NUST). On the one hand, the Boxtel Formation is made up of loamy fine sands with local silt, peat, or clay layers (TNO – Geological Survey of the Netherlands, n.d.[a]). On the other hand, the Sterksel Formation consists of coarse, gravelly sands (TNO – Geological Survey of the Netherlands, n.d.[d]). Beneath this subsurface, the first clayey layer is encountered. This layer forms the Formation of Breda (NUBRk1), a clay-rich unit composed of sandy clays and glauconitic fine sands (TNO – Geological Survey of the Netherlands, n.d.[b]). For this study, it is assumed this division forms the impervious layer forming the unconfined layer, and that this location at the creek is representative for the whole brook.

3.2. Data

In this subsection, the data used for this research and the validity testing is described. For the validity, the water balance and Budyko Framework tests are performed.

3.2.1. Meteorological and hydrological data

Data used for this research consists of meteorological and hydrological data. First, the meteorological data is presented, covering precipitation, short-wave radiation and evaporation. Thereafter, the hydrological data is described. This consists of soil water content, discharge, surface water level and groundwater level.

Meteorological data

KNMI has automatic weather stations across the Netherlands, one of which is situated in the Hupsel. Automatic measurement stations measure temperature, humidity, air pressure, wind speed and direction, precipitation, cloudiness, radiation and horizontal view (Koninklijk Nederlands Meteorologisch Instituut, n.d.). The meteorological observations are reported by KNMI on an actual basis (with a short delay of a few days) and are available from 1993 onward. For this case study, precipitation and short-wave radiation are utilized.

In addition to the KNMI observations, modelled potential and actual evaporation are obtained from GLEAM (Global Land Evaporation Amsterdam Model). The university of Ghent developed this model and estimates variables from satellite data. The potential evaporation is calculated with Penman’s equation through satellite data of surface net radiation, near surface air temperature, wind speed, vegetation height and vapor pressure deficit. With an evaporative stress factor, the actual evaporation and the different components that add up to this actual evaporation are estimated. The modelled interception loss, bare-soil evaporation and transpiration are taken from the GLEAM4.2a dataset. This dataset covers 1980–2023, with data from 1993 onward used in this study. The parameters have a daily temporal resolution and a spatial resolution of 0.1° by 0.1° (Gleam, 2024).

Hydrological data

As with modelled evaporation, the modelled soil water content is also obtained from the GLEAM4.2a dataset for the same time frame. The root-zone soil water content is chosen as the representative soil water content for the unsaturated zone. Water content is used as an indicator of relative soil moisture, since relative soil moisture is defined as water content divided by porosity, a parameter that is unknown and can vary between locations.

To assess drought conditions in the area, this study focuses on the most downstream point where all creek water passes through. At this point is an outlet called *Meetstuw* (Dutch for “measurement weir”). Waterschap Rijn en IJssel also uses Meetstuw as the official location name in their monitoring data. Accordingly, this study refers to the site as Meetstuw throughout the study, in line with the waterboard’s naming. Waterschap Rijn en IJssel provides measurements of discharge through the outlet and of

water levels upstream and downstream of the measurement weir. For this research, the discharge and water level upstream is utilized. The data span covers the years 1993 up to the present day. Furthermore, groundwater level measurements, which are used for the 3Di analysis are also provided from Waterschap Rijn en Ijssel. Three are provided from 2012 onward (Ten Barge, Meteoveld and Camping), following one more from January 2020 (Schoolweg) and one extra more from July 2020 onward (Eimersweg).

Table 3.1 gives an overview of all data used in this research with the time span, source and units. Both precipitation as well as discharge data are available from 1993 up to a few days before present, whereas modelled actual evaporation is only available until 2024. The analysis is chosen to cover the common and whole years, which corresponds to 1993 up to including 2023, a total time span of 30 years.

Table 3.1: Overview of data used in this study.

Variable	Time span	Source	Units from source
Precipitation	1993–present (used until 2023)	KNMI	$0.1\ \mathrm{mm/day}$
Radiation	1993–present (used until 2023)	KNMI	$\mathrm{J/cm^2/day}$
Potential & actual evaporation	1993–2023	GLEAM v4.2a	$\mathrm{mm/day}$
Soil water content	1993–2023	GLEAM v4.2a	$\mathrm{m^3/m^3}$
Discharge	1993–present (used until 2023)	Waterschap Rijn en IJssel (Meetstuw)	$\mathrm{m^3/s}$
Water level	1993–present (used until 2023)	Waterschap Rijn en IJssel (Meetstuw)	$\mathrm{m\ NAP}$
Groundwater level	2012–present (3 wells); 2020–present (2 additional wells); 2023–present (1 additional well)	Waterschap Rijn en IJssel (Ten Barge, Meteoveld, Camping, Schoolweg, Eimersweg)	$\mathrm{m\ NAP}$

3.2.2. Testing climate data validity

There are two tests conducted in order to test the validity of the data: the long-term water balance test and the Budyko Framework test. These tests are performed to ensure validity of the data, as they check that fluxes stay within physical limits and that the fraction of rainfall lost to evapotranspiration remains within the limits set by available water and energy. For these tests, data is required for precipitation from KNMI, potential and actual evaporation from GLEAM and discharge from the waterboard. The following equations describe the two tests:

Water balance
The conservation of mass of the brook can be written as:

$$\frac{dS}{dt} = P(t) - E_A(t) - \frac{Q(t)}{A} - L(t)$$

Where P is precipitation, E_A actual evaporation, Q discharge, A the area of the brook and L loss over time, all expressed as fluxes in mm/day. Since the discharge provided by the waterboard is given in m^3/s, it is converted to mm/day using the catchment area of Hupsel (6.97 km^2). Over the long-term when looking per year, the change in storage and losses are assumed to be negligible. This gives the long-term water balance:

$$\overline{P} - \overline{E_A} - \overline{\tfrac{Q(t)}{A}} \approx 0$$

Since potential evaporation E_P is always equal or larger than the actual evaporation E_A, the equation becomes:

$$\text{where} \quad \overline{P(t)} - \left(\overline{\frac{Q(t)}{A}} + \overline{E_P(t)}\right) \leq 0$$

This stricter constraint provides a robuster test of the water balance. The annual water balance is calculated for the 30 years of data by computing the mean daily values for each year representing the long-term conditions. Thereafter, the water balance equation is applied as described above. For each year, the condition if fulfilled, indicating that the water balance is closed for the whole time span of the Hupsel.

Budyko framework
For the Budyko Framework test, the fractions of precipitation that are evaporated and drained are determined. When rearranging the water balance, the equation becomes:

$$\frac{\overline{E_A(t)}}{\overline{P(t)}} = 1 - \frac{\overline{\frac{Q(t)}{A}}}{\overline{P(t)}}$$

Where the fraction of precipitation that is evaporated is named the evaporative index and the fraction of precipitation that reaches the river is named the run-off ratio.

In Figure 3.2, the evaporative index is plotted against the aridity index for each year. The ratio of means is also indicated in orange, this is the average of yearly mean potential evaporation divided by the average of yearly mean precipitation. The energy limit in red indicates the constraint that the actual evaporation must be smaller than the potential evaporation. In addition, the water limit in blue indicates the constraint that the actual evaporation should be smaller than precipitation. Since the water balance test shows that all data close the balance, this condition is automatically satisfied. Consequently, the governing constraint is that the evaporative index must be within the energy limit. As seen in Figure 3.2, no individual year shows actual evaporation exceeding potential evaporation. All the yearly data is thus suitable for analysis.

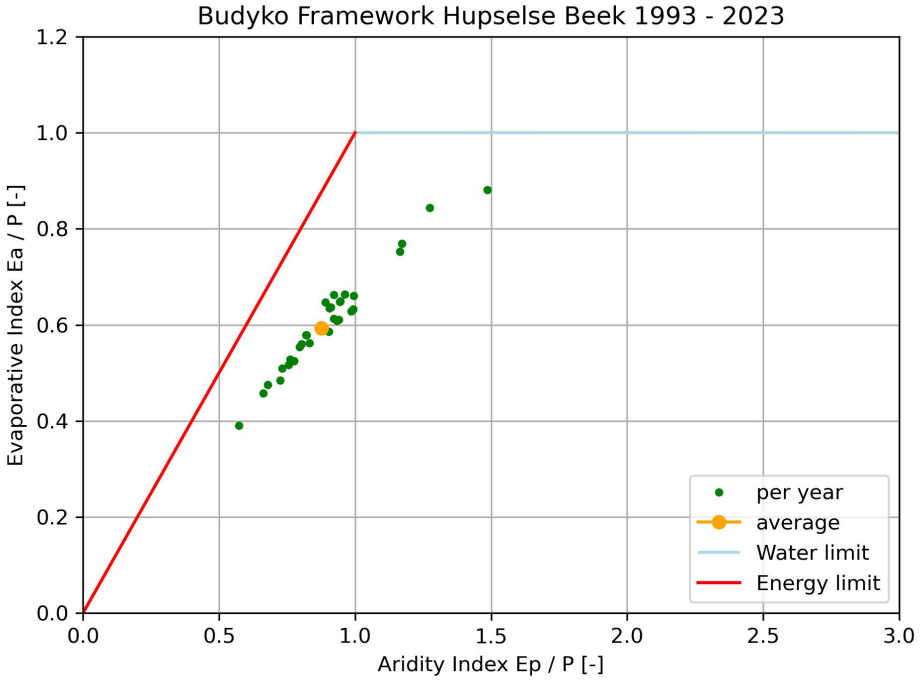

Figure 3.2: Budyko Framework of yearly data for the Hupselse Beek over the 1993–2023 period.

4

Methodology

This chapter outlines the methodology used for this research. The steps of this research are highlighted within three phases. The first phase consists of the data analysis, discussed in Section 4.1, where drought periods are selected and the correlation analysis is performed. The second phase introduces the bucket model, serving as an intermediate step that links the first to the second research question (Section 4.2). The final part, presented in Section 4.3, focuses on the 3Di modelling, detailing the steps required to set up the model, perform the simulations, and evaluate the results for the modelled drought events. A complete overview of all the steps in the methodology and how they link to the research questions is given in Section 4.4.

4.1. Data analysis

This section describes the method needed in order to answer the first research question, forming Phase 1 of this research. First, the steps required for the calculation of the standardized streamflow index (SSI) are discussed in Subsection 4.1.1. Thereafter, the process of finding the drought events through the drought index is described in Subsection 4.1.2. Next, Subsection 4.1.3 discusses how the correlation analysis is performed for all events while Subsection 4.1.4 focuses on the modelled 3Di events.

4.1.1. SSI calculation

As stated in Chapter 1, standard indices such as the Standardized Precipitation Index (SPI), Standardized Groundwater Index (SGI), and Standardized Streamflow Index (SSI) are commonly used to characterize drought severity. This study focuses on hydrological drought, as this type is able to capture the strongest transitions from dry-to-wet conditions. Therefore, the SSI is adopted. This index has been widely used to characterize streamflow drought and provide insights into drought severity and duration (Altayeb, 2023).

The SSI is used in order to select periods of hydrological drought within the 30 year time series of the Hupsel. The index is calculated for each specific calendar day by comparing streamflow values to historical values across multiple years. This requires a long data-set, typically a minimum of 30 years (Altayeb, 2023). The Hupsel discharge series meets this criterion. For this study, SSI-1 is used, representing the Standardized Streamflow Index with a one-month accumulation period. The one-month accumulation is obtained by applying a 30-day rolling average before fitting the distribution and computing the SSI. This helps reduce short-term fluctuations. For each calendar day across the years, a distribution is fitted. The fitted distribution can be empirical as well as parametric. While non-parametric methods may better fit the data, they tend to have higher uncertainty bounds. Additionally, with negative SSI values, they often underestimate both the magnitude and spread (Altayeb, 2023). In the study of Altayeb (2023), the SSI was determined for the Hupselse Beek based on simulated streamflow. The results of different fitted probability distributions were compared with each other. The Shapiro-Wilk normality test was applied, in which was concluded that the generalized extreme value (GEV) distribution was the best for simulated streamflow values. That is why this distribution is chosen for this study. The fit is assessed first before it is used, based on the analysis of the distribution function and the Q-Q plot. Next, the cumulative distribution function (CDF) is calculated. The last step is that these functions are converted into a standard normal distribution, which gives the SSI values.

Overall, these are the main steps for the calculation of SSI:

1. *Apply a 30-day rolling average* – For each day, the smoothed discharge per unit area $\overline{(Q/A)}_t$ is computed as the mean of the discharge values divided by the catchment area from the current day and the 29 preceding days. This reduces short-term fluctuations in the time series.
2. *Group by each day across all years* – The smoothed values are grouped by calendar day, resulting in 365 groups, one for each day of the year.
3. *Fit a distribution* – For each group, a probability distribution $F_d(x)$ is fitted to the sample values $\overline{(Q/A)}_t$. The Generalized Extreme Value (GEV) distribution is used primarily; if the fit is poor, alternative distributions are considered.
4. *Compute probabilities* – Each smoothed discharge per unit area $\overline{(Q/A)}_t$ is transformed into a cumulative probability using the fitted distribution:

$$p_t = F_d\left(\overline{\left(\frac{Q_t}{A}\right)}\right)$$

   where $p_t \in (0, 1)$ represents the probability of observing a value less than or equal to $\overline{Q}_t/A$ on day d.
5. *Standardize to SSI* – The probabilities are converted into standardized SSI values by applying the inverse of the standard normal CDF Φ^{-1}:

$$SSI_t = \Phi^{-1}(p_t).$$

   Here, $SSI_t < 0$ indicates drier-than-normal conditions, while $SSI_t > 0$ indicates wetter-than-normal conditions.

The fit of the GEV distribution is assessed based on the distribution function and the Q-Q plot. This is done for three days, January 1, May 2 and August 31, since they have approximately equal days apart. If this fit is poor, other distributions are considered.

4.1.2. Selection of droughts

After calculating the SSI, the next step is to identify droughts for the data analysis. To define these events, specific thresholds and criteria are applied. An SSI value below −1.0 is commonly used to define moderately dry hydrological conditions (Altayeb, 2023; Zalokar, Kobold, and Šraj, 2021; Wu et al., 2022). This SSI criteria is thus set as the threshold used to characterize hydrological droughts for the Hupsel data series. The minimum length for which this SSI has to remain below the threshold is not described in literature, as it is dependent on the study area. For this study, an initial duration of 25 days is adopted. An exception of up to five days is allowed in which the SSI may temporarily rise above –1.0, as such short fluctuations do not necessarily indicate the end of a drought event. The criteria are changed depending on the quantity of the results. Furthermore, peak discharge is identified as the maximum discharge in the period. This period extends from the start of the drought to its end, with an additional 15 days included to account for the lag between the system wetting up again and the occurrence of peak flow following a rain event.

4.1.3. Correlation analysis

For all drought events selected in Subsection 4.1.2, a correlation analysis is performed to answer the first research question. The relationship between antecedent soil moisture and peak discharge is examined using two approaches: an event-based analysis and a rolling-window analysis. To account for differences in rainfall intensity, peak discharges are expressed as run-off ratios.

First, the event-based analysis is performed. The run-off ratio is calculated by summing discharge and precipitation over the continuous sequence of rainy days containing the peak discharge, and dividing total discharge by total precipitation in that period. Furthermore, the antecedent soil water content value is obtained from one day prior to the start of the rainy period containing the peak discharge. With this antecedent soil moisture and run-off ratio, the correlation analysis is performed. The drought events are classified by season to investigate seasonal patterns. Winter is defined as December–February

and summer as June–August, with the remaining months classified as “other”. For comparison, non-drought peak discharge events are also included, defined as the highest discharges in the Hupsel record with a minimum spacing of 20 consecutive days, excluding peaks occurring during drought.

Next, the rolling-window analysis is conducted. The correlation analysis is performed per drought event in order to capture the dynamics for each drought and how these evolve over time. Therefore, every day of the drought is set as a starting point. Here, the soil water content is defined. Thereafter, from this starting point, the analysis considers the subsequent five-day window in which the run-off ratio is calculated.

4.1.4. Selection drought events for 3Di

From the drought events identified in Subsection 4.1.2, three are selected for modelling in 3Di. Because 3Di simulations require a long duration time, the simulation is limited to one week. The start and end dates are chosen so that intense rainfall is included, with drought conditions as the initial state. The selection criteria focus on relatively recent events, which have more surface and groundwater measurements, and on summer events, as these tend to be the most severe. Of the selected events, the most recent is used for model calibration, as it has the most data available, while the others are used for validation.

4.2. Bucket model

Recent studies have coupled hydrological models with hydrodynamic models. For instance, in the study of Xu et al. (2024), a hydrological model was used to simulate peak flow and flood volume. This was served as input for a hydrodynamic model for spatial extent and flood inundation simulations. Furthermore, in the study of Zhang et al. (2024), the two different model types were coupled through flow discharge to estimate flood processes. For this research, conceptual hydrological bucket models are linked with a hydrodynamic model in 3Di. The selected drought events from Subsection 4.1.2 are fed into hydrological bucket models using precipitation data as input. This forms Phase 2 of this study.

Three conceptual bucket models are given in Figure 4.1 in order to present the approach for the hydrological modelling. The complete bucket model that includes the roles of vegetation and soil moisture is visualized in Figure 4.1a. The unsaturated zone is modelled as an unsaturated bucket with storage S_U and the interception is modelled as the bucket with storage S_I. The precipitation P first intercepts on the canopy and becomes effective precipitation after that (P_E). From this part, there is a fraction that can be stored in the unsaturated zone, forming R_U. The remaining fraction is the part that cannot be stored in the unsaturated zone and forms the recharge R. This part splits into lateral recharge R_L and fast groundwater recharge R_F. Because of sandy soil conditions, slow percolation is considered negligible and is therefore not accounted for. The dataset from GLEAM provides data for different evaporation components. Interception bucket has interception evaporation E_I and the evaporation of the unsaturated zone bucket E_T is composed of transpiration and bare soil evaporation.

Additionally, Figure 4.1b and Figure 4.1c give reduced forms of the bucket model given in Figure 4.1a. The output of these simplified models serve as input for the 3Di model. Specifically, 3Di is run with effective precipitation (Figure 4.1b), representing the fraction of rainfall not stored as interception, and recharge (Figure 4.1c), representing the fraction of rainfall also not retained in the unsaturated zone. The first input is used to investigate how 3Di simulates peak flow after drought when interception is accounted for, while the second input tests whether using only the portion that cannot be stored in the unsaturated zone leads to more accurate results.

For both reduced bucket models, balance equations are obtained by drawing control volumes around the interception bucket and the unsaturated zone bucket (including the splitter). These result in Equation 4.1 and Equation 4.2. The recharge from the unsaturated bucket R depends on $S_{U,\max}$ and β, which relates to the maximum capacity and the released part of $S_{U,\max}$ respectively. The storages S_I and S_U cannot be negative and are constrained by their maximum storages $S_{I,\max}$ and $S_{U,\max}$ respectively. Because of this constraint, and since β is positive, R is bounded by 0 and P_E.

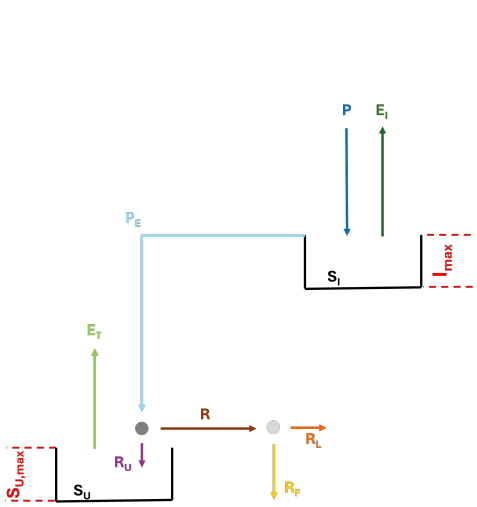

(a) Bucket model including interception and unsaturated zone.

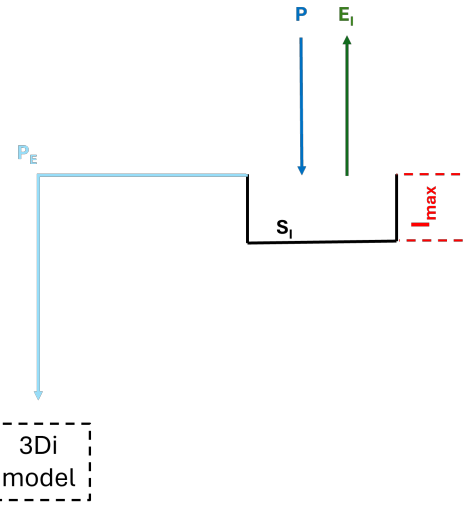

(b) Reduced bucket model: effective precipitation input for 3Di.

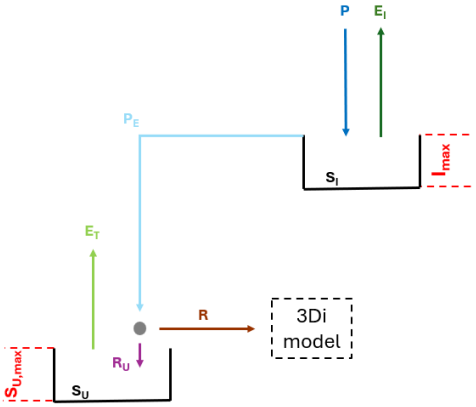

(c) Reduced bucket model: recharge input for 3Di.

Figure 4.1: Comparison of three bucket model variants. Figure 4.1b and Figure 4.1c show the method used for this research while Figure 4.1a is for illustrative purposes.

$$\frac{dS_I}{dt} = P - E_I - P_E \tag{4.1}$$

$$\frac{dS_U}{dt} = P_E - E_T - R = P_E - E_T - \left(\frac{S_U(i-1)}{S_{U,\max}}\right)^{\beta} P_E \tag{4.2}$$

With these expressions, and under the assumptions that β and $S_{U,\max}$ are fixed parameters and that the storage buckets are empty at the initial time step, the effective precipitation P_E and recharge R can be calculated iteratively for each time step. The time step is chosen to be set hourly for the most accurate results. To obtain hourly values, the evaporation components from GLEAM are scaled from mm per day to mm per hour. The hourly evaporation is scaled through multiplying the total evaporation on that day with the fraction of radiation in that hour over the total radiation on that same day. This approach assumes that evaporation is proportional to incoming radiation, the effects of vapour pressure deficit, humidity, wind speed and temperature are neglected.

In the study of Espinoza et al. (2024), the calibration range for β is between 1.0 and 6.0 mm. A larger value of $S_{U,\max}$ and/or β leads to decrease in outflow of the unsaturated zone (Espinoza et al., 2024). This indicates that higher values of β and $S_{U,\max}$ lead to slower drainage, which is influenced by soil properties. Sandy soils drain quickest and clay soils the longest. Since the soil mainly consists of loamy sand and a bit of clay, peat, and gravel, the value of 2.0 mm is chosen for β. This value lies towards the

lower end of the range due to main sandy conditions, but is kept slightly higher to account for the clay content. For the other parameters buckets $S_{I,\text{max}}$ and $S_{U,\max}$, the initial value is estimated to be 2.0 mm and 50 mm respectively. An ensemble analysis is performed with three different values of $S_{U,\max}$: 50, 100 and 150 mm.

4.3. 3Di model set-up

In Phase 3, the final phase of the research, a 3Di schematization of the Hupselse Beek is developed. This schematization contains data and parameters needed to construct a 3Di model, a format with computational grid to run calculations. The peak flow of the calibration and validation events is tested using the same 3Di schematization, except for the initial conditions. The inputs consist of the hourly effective precipitation P_E and recharge R for each value of $S_{U,\max}$, as derived in Section 4.2. These forcings are applied in the 3Di model, which then produces the simulation results. The parameters and data required for the schematization and model is described in Subsection 4.3.1. Thereafter, Subsection 4.3.2 presents the calibration method, which can follow either a spatially lumped or a distributed approach. It also describes how the different simulations are tested and how their performance is assessed.

4.3.1. Schematization and model

This subsection describes the model objects and settings used in 3Di to represent the Hupselse Beek. These elements show how 3Di translates the physical characteristics of the catchment into a computational model. More information about model set-up in 3Di can be found in the 3Di documentation website (Nelen & Schuurmans, 2025).

Setting objects

A high-resolution Digital Elevation Model (DEM) from Actueel Hoogtebestand Nederland 4 (AHN4) is loaded, featuring a spatial resolution of 0.5 m x 0.5 m. This elevation data is derived from laser altimetry, with approximately 10 elevation measurements recorded per square meter. The DEM is modified so that the channels are embedded into the terrain. This is necessary because laser altimetry reflects the water surface rather than the channel bed, resulting in inaccurate elevation data for watercourses. In addition, a file containing surface Manning friction coefficients is included. The raster is derived from a land use map provided by Nelen & Schuurmans.

Furthermore, the computational and vertical resolution is specified in the settings. For the computational resolution, the minimum cell size chosen is 10 m x 10 m with 3 grid cell levels. This means that refined locations have 10 m x 10 m grid cells, with the cell size doubling at each level further from the refinement.

Groundwater settings

As stated in Section 3.1, the loamy sand layer in the Hupselse Beek area varies in thickness from 0.2 to 10 m and rests on an impermeable clay layer. In 3Di, a spatially varying impervious layer can be added. However, due to uncertainties in how this level varies across the area, the base of the unconfined aquifer is assumed to be uniform. This level is determined based on the vertical cross-section from BRO REGIS II from DINOloket (Appendix B) at the location of the main creek, which is approximately 21.8 m NAP. The assumption of an impervious layer is supported by the elevation range of 22 to 35 m NAP (derived from the DEM raster) and by the loamy sand layer depth of 0.2 to 10 m. This assumption is consistent with the idea that lower elevations are associated with lower depths and higher elevations with higher depths.

Next to the impervious layer, the effective porosity, hydraulic conductivity and Horton infiltration parameters are set. These parameters differ per soil type. The values are based on literature and adjusted within calibrated ranges specific to the soils in the Hupsel, which consists primarily of loamy sand and a bit of clay, peat, and gravel. First, the ranges for effective porosity are defined. The paper of Urumović and Urumović Sr. (2016) gives a relationship between referential grain size and effective porosity. The data was examined for samples from clay to gravel. Different soil types show different ranges in effective porosity: for silt and clay 0.03–0.08; for sand this range is 0.25–0.35; and for sandy gravel 0.27–0.33. Since the Hupsel soil is primarily made up of sand, the upper bound is chosen to be set at 0.35. The lower bound is set at 0.10 since the addition of clay and silt decreases the effective porosity. For the initial simulation, the effective porosity is set at 0.23, the average of the two extremes.

Thereafter, the calibration ranges for hydraulic conductivity are determined. In the study of Yusuf et al. (2020), the hydraulic conductivity for loamy sand was determined for two different tests and at four different depths. Mean values ranged from 8.3 m/d at a depth of 0.02 m to 0.40 m/d at a depth of 0.06 m. Furthermore, the study of Lee et al. (1985) measured the saturated hydraulic conductivity for different soil types and with three different measurement techniques in Ontario, Canada. Averaged over the three methods, this gave values of 2.6 m/day for sand and 0.17 m/day for loam. Given that there is a large range of values for hydraulic conductivity, the calibration range is chosen between 0.1 and 10 m/d. The geometric mean of the two extremes, equal to 1.0 m/day, is chosen as the base value before calibrating. This is supported by previous work, where both Prudic (1991) and Chen et al. (2018) report that their hydraulic conductivity data follow a log-normal distribution and apply the geometric mean as a representative measure.

Unlike effective porosity and hydraulic conductivity, there is limited literature available on Horton infiltration parameter values. For this thesis, the study by Gilliom et al. (2019) serves as the only source, providing Horton parameter values per soil group. The initial parameter is set based on loamy sand, with an initial infiltration rate of 25.4 mm/h, an equilibrium infiltration rate of 5.1 mm/h and a decay rate of 3 hours. Based on model performance using these values, the parameters are either increased or decreased through interpolation between loamy sand and either the higher soil class type sandy loam or the lower soil class clay. This ensures that physically realistic differences between initial and equilibrium infiltration rates remain as reported in literature. Throughout the calibration procedure, the decay rate of 3 hours is kept constant, as all soil types except for sand are reported to show similar values in the study of Gilliom et al. (2019).

A complete overview of the chosen groundwater setting parameters is given in Table 4.1, where the calibrated values are shown in bold. The calibrated procedure is further described in Subsection 4.3.2.

Groundwater settings in 3Di	Value	Unit	Explanation
Impervious layer level	21.8	m NAP	From DINOloket
Initial infiltration f_0	**610**	**mm/day**	**Value loamy sand**
Equilibrium infiltration f_{eq}	**122**	**mm/day**	**Value loamy sand**
Infiltration decay k	3	hour	Value loamy sand
Effective porosity ϕ_{eff}	**0.23**	**[-]**	**Mean 0.10 – 0.35**
Hydraulic conductivity K	**1.0**	**m/day**	**Geometric mean 0.10 – 10**

Table 4.1: Initial groundwater settings with calibrated settings in bold.

Initial conditions
The initial conditions are specified for both groundwater and surface water. For groundwater, observations at different locations make initialisation possible for the calibration and validation events. For surface water, however, there is only one measurement point at Meetstuw. Therefore, initialisation relies on an assumption that is the same for all events.

The distribution of initial groundwater levels within the area is based on the Average Lowest Groundwater Level (GLG) map. This corresponds to the 30-year average of the LG3, which represents the mean of the three lowest groundwater measurements per hydrological year, based on bi-monthly observations. In the map, groundwater levels are expressed as depths relative to the ground surface. Because the DEM has higher pixel accuracy, the GLG raster is first projected. A draft raster is then created by subtracting the depth of groundwater level from the DEM. Initial levels are further tweaked, depending on the measurements provided by the waterboard. Figure 4.2 illustrates the resulting initial groundwater level raster for 2023.

Additionally, an initial surface water level is defined. As there is only one downstream measurement of water level at Meetstuw, the water levels in the rest of the channels are unknown. It is assumed that the water level along the creek reflects dry conditions and is therefore raised by 0.60 m at the lowest elevations.

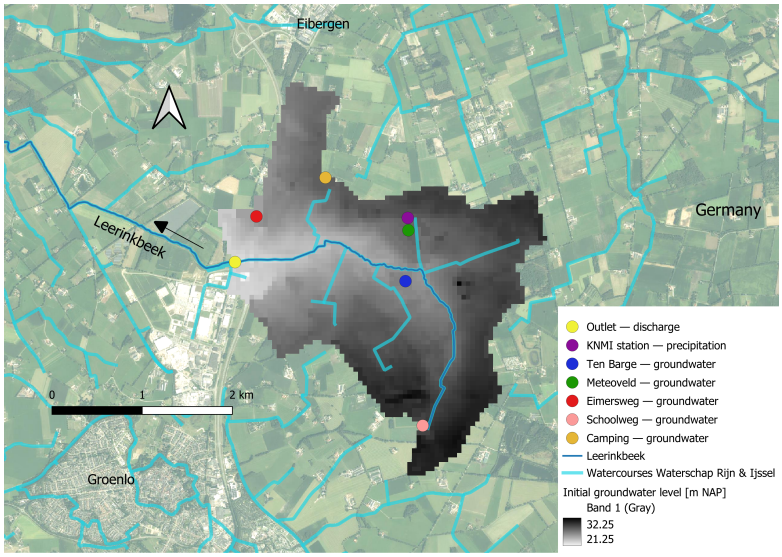

Figure 4.2: Initial groundwater level raster for 2023 for study area. Aerial image obtained from the WMS service Actueel Ortho25 with a resolution of 25 cm is used to map the background. Water courses are illustrated with lines and measurement points with dots.

1D objects

The creek of the Hupselse Beek, represented as 1D channel objects in 3Di, is added to the schematization. For these channels, cross section locations are defined. At these sections, the channel geometry is specified along the Y–Z plane. There are a total of 157 measured and theoretical profiles provided by Waterschap Rijn & Ijssel. In between these defined locations, the cross section profile is interpolated along the watercourses. These have $K_{\text{Strickler}}$ friction values available that range between 15 and 25 depending on the cross-section. An average value of 20 is used across all channel sections. Since only Chézy or Manning friction type is required, this $K_{\text{Strickler}}$ is converted to Manning. According to Ankum (2002), for uniform flow, $K_{\text{Strickler}}$ = 1 / n for uniform flow. This gives a value n of 0.05. With these cross-section locations, the channels are added. Lastly, connection nodes are placed, representing locations where the 1D and 2D domains exchange.

Next to the channels, hydraulic structures are added. In the Hupselse Beek, there are 51 culverts and 10 weirs. The culverts are represented as 1D objects, while the weirs are represented as 2D obstacles, as explained in the next section. Short-crested orifices are placed instead of culverts to simplify the complex flow dynamics which you would need when modelling culverts. The cross-sections of the culverts are mostly circular, with some rectangular, and the discharge coefficients are assumed to be 0.8. To model the culverts, data from the waterboard is used, providing upstream and downstream invert levels (m NAP) as well as cross-sectional dimensions (width and height). Since the orifice formulation requires a crest level, the upstream invert level is taken as the lowest point of the opening, so that flow starts once water covers the culvert bottom. Missing data is completed from measurements on the field during a site visit with a staff gauge.

2D objects

In the 3Di schematization and model, the ten weirs are represented as obstacles. The function of an obstacle is to impose a fixed crest level on the computational grid, ensuring that water can only pass once this elevation is reached. The obstacle is implemented as a line with a crest level, which overrides the DEM values at the cell edges when calculating cross-sections between adjacent cells, if those values are lower (Nelen & Schuurmans, 2025). For this 3Di model, the crest levels are assumed to correspond to the lowest elevation of the weirs.

In addition, a grid refinement line is added along the channels in the 3Di model, allowing the model to calculate most accurately in this region. This level is referred to as level 1. The minimum cell size that is specified in the model settings is 10 m x 10 m. As specified in the model settings, the model allows up to three grid levels. This means the computational grid is four times larger (20 m x 20 m) in the areas around the channel and 16 times larger (40 m x 40 m) in the areas further away, corresponding to level 2 and level 3 respectively. This last level makes up most of the computational grid.

Lastly, a 2D boundary condition is applied for the 2D surface domain. A downstream water level boundary is set downstream of Meetstuw with a low water level (-999 m NAP) to allow outflow. For groundwater, no boundary condition is applied due to insufficient data on subsurface flow in the area.

4.3.2. Calibration, simulation and analyzing results

A sequential calibration is performed on the most recent drought event, as it contains the most groundwater data. Model parameters are adjusted based on performance, and the final calibrated values are then applied to two other drought events for validation. The sequential calibration focusses on faster processes prior to slower flow and storage parameters like effective porosity and hydraulic conductivity. The parameters that are calibrated are given in Table 4.2, with their initial values. First, the Horton infiltration parameters (initial and equilibrium infiltration rates) are calibrated to the surface water measurements, as these primarily control the amount of water that infiltrates from precipitation and are not directly influenced by effective porosity or hydraulic conductivity. Next, effective porosity is calibrated to match groundwater storage dynamics, focusing on the amplitude of groundwater rise. Finally, hydraulic conductivity is tuned to reproduce groundwater gradients and lag times between upstream and downstream observations. Both effective porosity and hydraulic conductivity are calibrated using the groundwater observations.

In 3Di, parameters can either be specified as uniform values, representing a spatially lumped model, or as spatially varying rasters in a distributed approach. Because effective porosity and hydraulic conductivity span a wide range of values, a lumped representation may in some cases provide more robust calibration results. Calibration is initiated with uniform values for all parameters. Depending on these results, it is investigated whether changing to spatially varying rasters can lead to better results.

Groundwater settings in 3Di	Value	Unit	Explanation
Initial infiltration f_0	610	mm/day	Value loamy sand
Equilibrium infiltration f_{eq}	122	mm/day	Value loamy sand
Effective porosity ϕ_{eff}	0.23	[-]	Mean 0.10 - 0.35
Hydraulic conductivity K	1.0	m/day	Geometric mean 0.10 - 10

Table 4.2: Parameters used for sequential calibration.

Figure 4.3 builds on Figure 2.1 presented in Chapter 2, showing the two model domains together with the groundwater parameters, with the calibrated values indicated by circles. The figure illustrates the structure of the model, in which both effective precipitation P_E and recharge R serve as inputs.

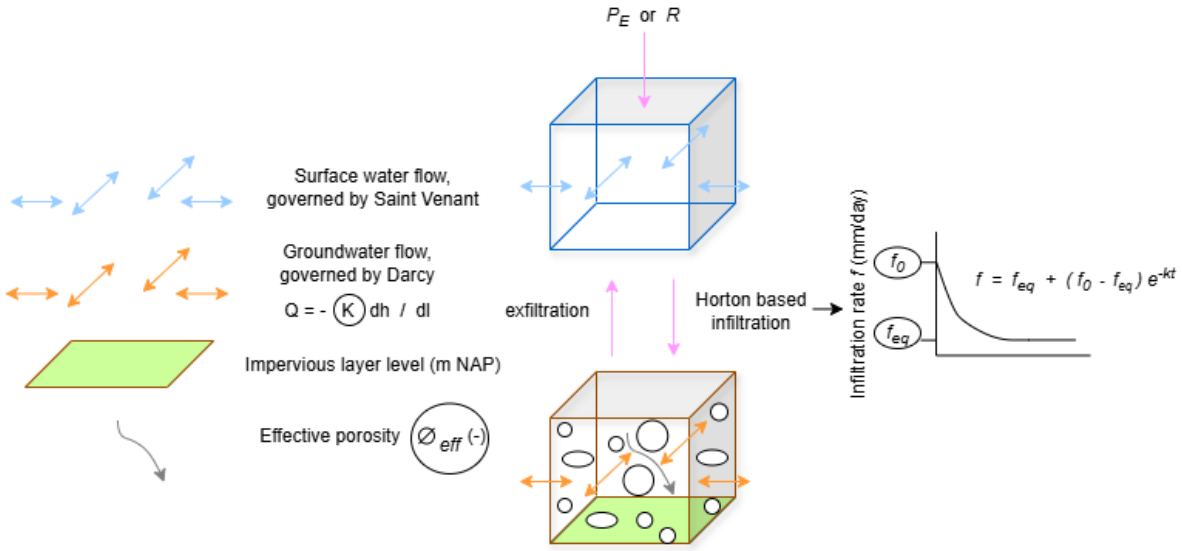

Figure 4.3: 3Di cells: upper for surface water elevation domain and lower for groundwater domain. Calibration parameters are circled. Figure inspired from slides for 3Di training. (Volp, 2025)

During the calibration procedure, the performance of the results for groundwater and surface water are assessed with to the following key metrics: NSE, $RMSE$, $logNSE$, R^2 and KGE. Table 4.3 gives an overview of the metrics with their formula, description and application for this research.

Table 4.3: Overview of key metrics used for model evaluation of surface water and groundwater levels. Here, h_t^{obs} and h_t^{sim} are observed and simulated water levels at time t; $\overline{h}^{\text{obs}}$ and $\overline{h}^{\text{sim}}$ are their means; r is the linear correlation coefficient; σ the standard deviation; and N the total number of time steps. Water levels h have units $[L]$ (reported as m NAP).

Key Metric	Formula	Description	Application for this research
Nash–Sutcliffe Efficiency (NSE)	$1 - \frac{\sum(h_t^{\text{obs}} - h_t^{\text{sim}})^2}{\sum(h_t^{\text{obs}} - \overline{h}^{\text{obs}})^2}$	Goodness of fit relative to the observed mean (1 = perfect, 0 = mean benchmark, < 0 worse).	Assess goodness of fit between observed and simulated water levels.
Log-transformed NSE (logNSE)	$1 - \frac{\sum(\log h_t^{\text{obs}} - \log h_t^{\text{sim}})^2}{\sum(\log h_t^{\text{obs}} - \overline{\log h^{\text{obs}}})^2}$	Variant of NSE applied on log-transformed data, giving more weight to low flows.	Evaluate model fit for low-flow conditions in groundwater.
Kling–Gupta Efficiency (KGE)	$1 - \sqrt{(r-1)^2 + (\alpha-1)^2 + (\gamma-1)^2}$, $\alpha = \frac{\sigma_{h^{\text{sim}}}}{\sigma_{h^{\text{obs}}}}$, $\gamma = \frac{\overline{h}^{\text{sim}}}{\overline{h}^{\text{obs}}}$	Combines correlation r, variability ratio α, and bias ratio γ.	Balanced assessment of timing, variability, and bias in water levels.
Root Mean Square Error (RMSE)	$\sqrt{\frac{1}{N}\sum(h_t^{\text{obs}} - h_t^{\text{sim}})^2}$	Average error magnitude (penalizes larger errors).	Quantify typical water level error (m).
Coefficient of Determination (R^2)	$\left(\frac{\sum(h_t^{\text{obs}} - \overline{h}^{\text{obs}})(h_t^{\text{sim}} - \overline{h}^{\text{sim}})}{\sqrt{\sum(h_t^{\text{obs}} - \overline{h}^{\text{obs}})^2 \sum(h_t^{\text{sim}} - \overline{h}^{\text{sim}})^2}}\right)^2$	Proportion of variance in observations explained by simulations.	Check how well temporal variability in water levels is reproduced.
Percent Bias (PBIAS)	$100 \cdot \frac{\sum(h_t^{\text{sim}} - h_t^{\text{obs}})}{\sum h_t^{\text{obs}}}$	Average tendency of simulations to overestimate or underestimate observations (in %).	Quantify relative bias in simulated water levels.

4.4. Methodology overview

The complete methodology is given in Figure 4.4. The correlation analysis that is performed in Phase 1 answers research question 1. Furthermore, the last step in Phase 3 answers research question 2 and 3. Research questions 2 and 3 are distinguished by the simulation input, which is effective precipitation P_E in the case of research question 2 and recharge R in the case of research question 3. These inputs from the bucket model are highlighted through the arrow that links the bucket model step from Phase 2 to the calibration, simulation and analyzing results step in Phase 3. For Phase 3, the schematization and model can be constructed independently of Phase 1 and 2 since the study area is defined. The only dependency is that the initial groundwater conditions rely on the selection of drought events for 3Di in Phase 1. This is also indicated by a black arrow.

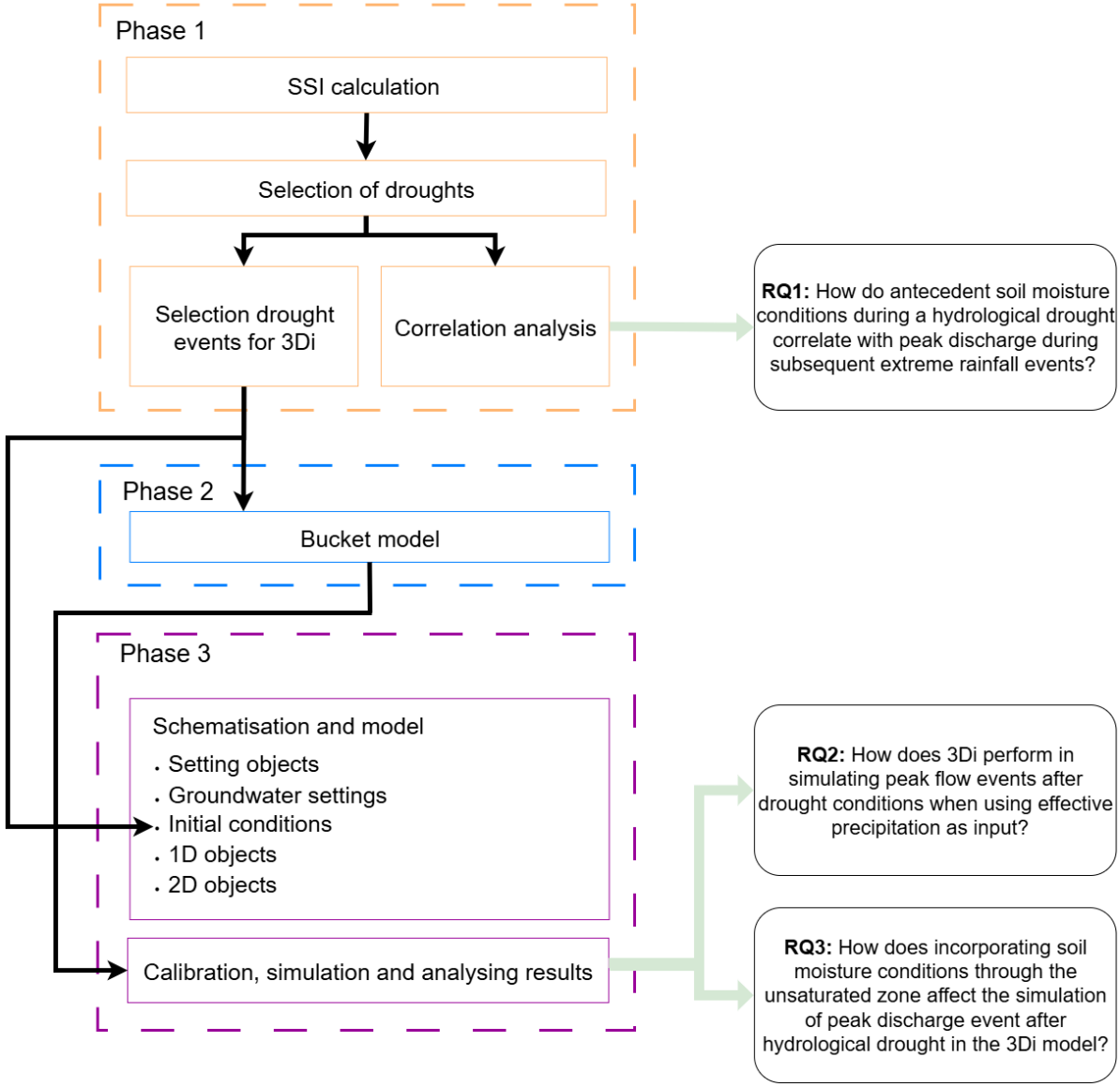

Figure 4.4: Flow diagram that gives overview of the methodology structure. Boxes with solid lines represent the methodological steps, whereas dashed-line boxes indicate the corresponding phases. The green arrows highlight how each step contributes to answering the research questions. If a step is dependent of another one, it is linked with a back arrow. The green arrows highlight which steps contribute to answering the research questions.

5

Results

This chapter provides the results for this research. Section 5.1 examines how antecedent soil moisture correlates with peak discharge, covering Phase 1 of the research. Section 5.2 highlights the 3Di model performances from simulations for the chosen post-drought events (Phase 3). The steps from Phase 2 are indirectly incorporated in Section 5.2, as they define the model inputs.

5.1. Data analysis

This section discusses the results of the data analysis. First, Subsection 5.1.1 presents the results of the GEV fit to the streamflow values and the subsequent calculation of the SSI. The selected droughts that follow from the criteria are presented in Subsection 5.1.2. Thereafter, the correlation analysis for the different droughts followed by peak events is reported in Subsection 5.1.3. Of these droughts, the selected ones that are simulated in 3Di are given in Subsection 5.1.4.

5.1.1. SSI calculation

To calculate the SSI for each day within the time series, a probability distribution is fitted to the streamflow data. The GEV distribution is assumed to provide the best fit for the SSI, and its performance is evaluated for three days. The empirical distribution and Q-Q plot are analyzed, as illustrated in 5.1. The upper plots show a histogram with the GEV fit. Here, the x-axis represents the 30-day rolling mean discharge $Q_{30\text{day}}$ expressed in mm/day. The y-axis shows the probability density, where the histogram represents the empirical distribution of discharge values and the red curve represents the fitted GEV distribution. The lower plots illustrate Q-Q plots, where the empirical quantile derived from observed streamflow data is plotted against the quantiles predicted by the GEV distribution.

Histograms show a moderately skewed distribution for January 1, followed by a bit right-skewed distribution for May 2 and a large skewed distribution with a sharp peak near zero for August 31. The points generally align well with the 45-degree line in the Q-Q plot. There are some deviations in the upper tail, especially for May 2 and August 31.

The GEV distribution provides a generally good fit for the data. Although there are some outliers for the high flows, this does not significantly affect the application of the fit. Since the GEV fit is used to identify droughts, and not peak flows, these outliers will not interfere with the analysis.

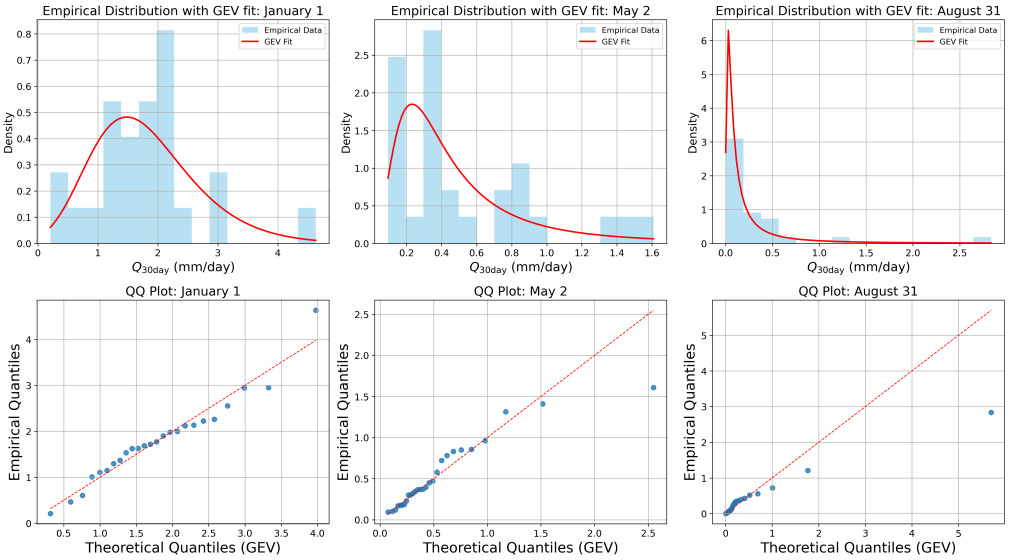

Figure 5.1: Empirical distribution and Q–Q plot GEV fit January 1, May 2 and August 31.

With the accepted GEV as distribution, the SSI is calculated. Figure 5.2 illustrates the results for this SSI method for the years 1993 up to and including 2023. The gaps indicate that there is missing discharge data on that day.

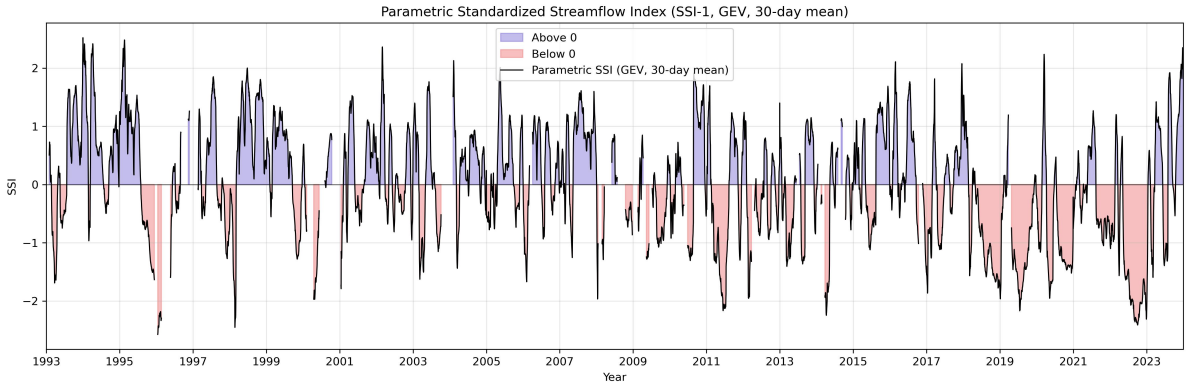

Figure 5.2: SSI index Hupselse Beek.

5.1.2. Selection of droughts

With the calculated SSI, the initial criteria described in Subsection 4.1.2 is set in order to find drought events. During this process, it is discovered that the criteria of SSI smaller than -1.0 is too stringent. An SSI threshold of -0.5 leads to around 65 percent more events. Therefore, this criteria is changed, resulting in 38 drought events. Of these, eight are in summer, twelve in winter and the rest in the other months. In addition, the top 28 highest peak events that are not preceded by a drought are identified.

5.1.3. Correlation analysis

The event-based correlation analysis is performed for all 48 drought events and 28 highest peak events, not followed by hydrological droughts. The run-off ratio is plotted against the antecedent soil water content prior to the peak event and shown in Figure 5.3. The plot highlights a threshold at around a soil water content of 0.22 mm^3/mm^3. Below this threshold, the Q/P ratios range between 0 and 0.2. Conversely, above the threshold, the Q/P ratios increase faster. Linear regression lines are plotted to stress the threshold.

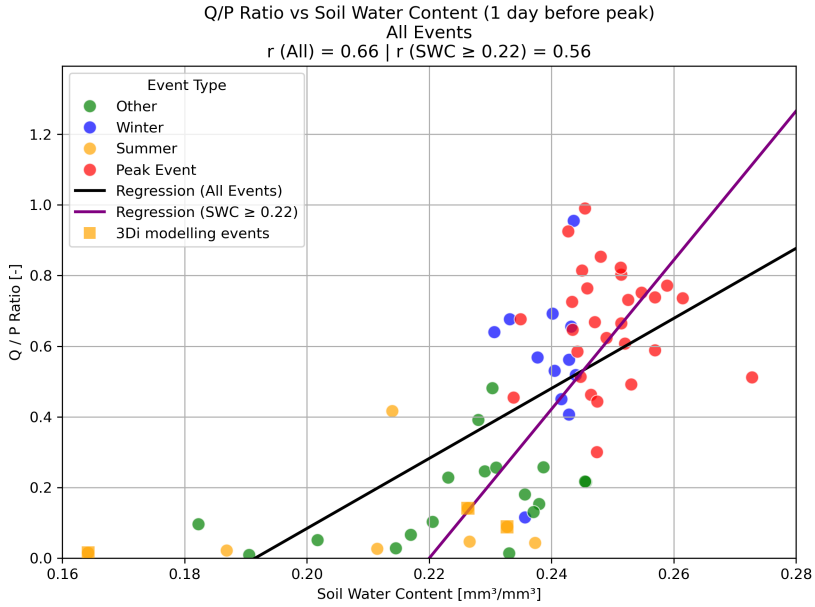

Figure 5.3: Correlation between run-off ratio (Q/P) and soil water content (SWC) one day before the peak event. Green, blue, and yellow markers show peaks following drought, while red markers show peaks not preceded by drought. The black regression line is for all events, and the purple line is for events with $SWC \geq 0.22$.

Additionally, the rolling-window analysis is conducted, in which the correlation analysis is performed for individual droughts. All the plots are given in Appendix C for summer and Appendix D for winter. For illustrative purposes, some examples are given in Figure 5.4. From these results, it is clear that there is a difference between winter and summer. In summer, soil water content varies over a wider range, and the threshold effect is more pronounced compared to winter, where the data points align more vertically. Four events show notably lower soil water content values. These correspond to long drought periods (around half a year), where the drought began in summer and soil water content was already low at the start.

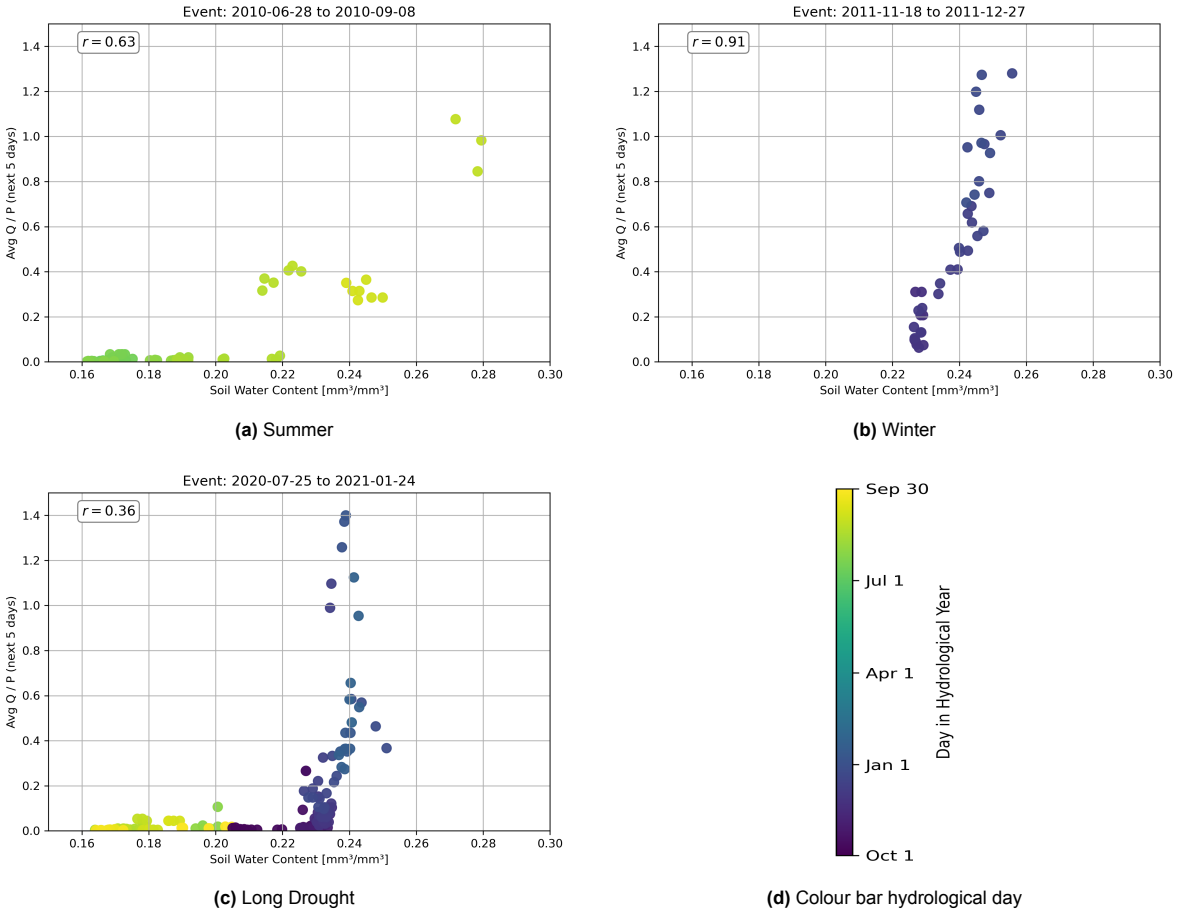

(a) Summer

(b) Winter

(c) Long Drought

(d) Colour bar hydrological day

Figure 5.4: Results for rolling-window analysis. Plots show average run-off ratio against antecedent soil water content for summer drought (a), winter drought (b) and long drought (c). All other plots are given in Appendix C for summer and Appendix D for winter. The colour-coded bar (d) indicates the date.

5.1.4. Selection drought events for 3Di

Of the total eight summer drought events, three summer events are selected for modelling in 3Di. Events from 2012 onward only are suitable for modelling in 3Di since these contain groundwater data. Of these summer events, four are from 2012 onward (2012, 2015, 2020 and 2023). The first is chosen not to model since the peak discharge is the lowest of the three and occurs before the lowest SSI. Illustrations of the three most recent summer droughts (2015, 2020, and 2023) are provided in Appendix E. For each drought period, plots are given for precipitation, evaporation, discharge with SSI, soil water content, surface water level and groundwater level. Since 2023 has the most data on groundwater measurements, it is used as the 3Di calibration event. The events of 2020 and 2015 are used to validate the model.

5.2. 3Di

The input that is used for the effective precipitation and the recharge with three different $S_{U,\max}$ parameters and for the years 2015, 2020 and 2023 are given in Appendix F, Appendix G and Appendix H respectively. It is highlighted that the event of 2015 is mostly cumulative and has the smallest maximum effective precipitation per hour. Conversely, the event of 2020 has the highest maximum effective precipitation per hour and is the most instantaneous one. Lastly, the event of 2023 is the most continuous peak event, with effective precipitation occurring each day. When adding the bucket, decrease in hourly recharge is noticeable and impact differs per peak event. For instance, for the week in 2020, the first instantaneous peak has largest decrease since the bucket is assumed to be empty.

The following subsections report the results following the calibration and validation procedures. These results for calibration are presented for effective precipitation in Subsection 5.2.1 and recharge in Subsection 5.2.2. Thereafter, Subsection 5.2.3 and Subsection 5.2.4 depict the validation results for effective precipitation and recharge respectively. For the calibration steps, the intermediate results are reported in the appendix, where corresponding water balance schematics are also included.

5.2.1. Calibration effective precipitation

Base simulation

Before calibration, the base simulation is run. The results for both surface water at Meetstuw and the five groundwater locations are given in Figure 5.5. The plots and key performance metrics show that the groundwater simulations perform better compared to the surface water. For instance, the differences in R^2 indicate that the model can explain the variance in the observed data much more for groundwater compared to surface water. For all locations, NSE and $logNSE$ values are relatively close, suggesting that the model performs comparably for both low flows and peak flows. The relatively high values of NSE, $logNSE$ and $logNSE$ for the Camping site show that the groundwater is already well represented by the model, while others suggest further optimisation. In addition, for groundwater, the model underestimates for two sites (Ten Barge and Meteoveld), while it overestimates for the three other sites (Camping, Schoolweg, Eimersweg).

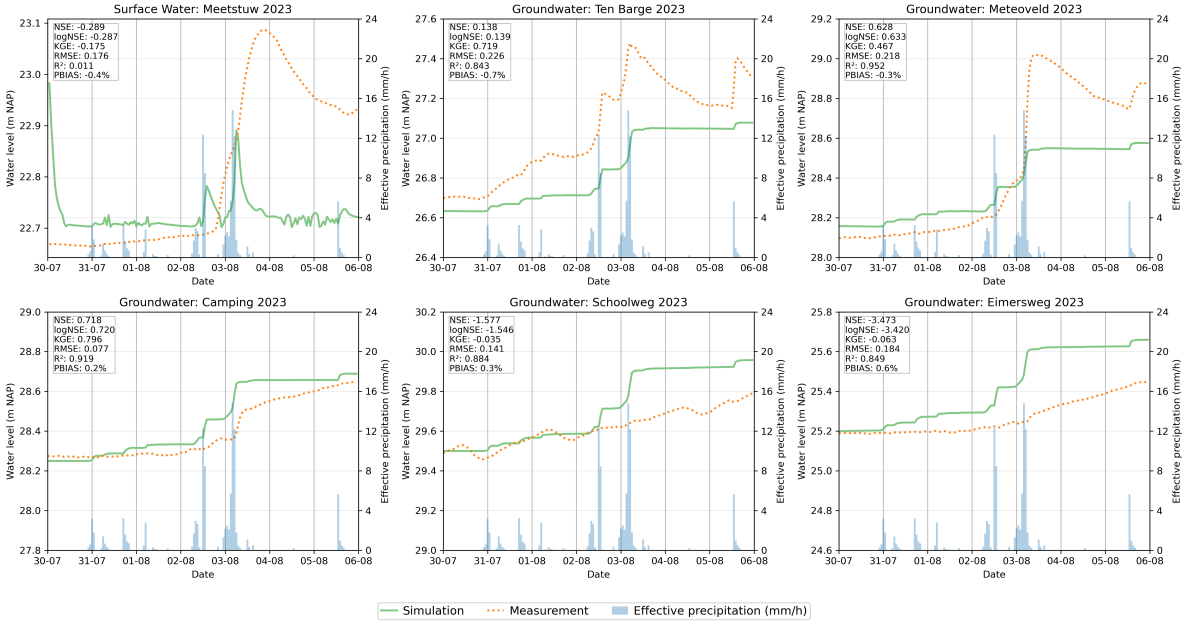

Figure 5.5: Base simulation with initial values for 2023 calibration event. Upper left is surface water at Meetstuw, followed by the four groundwater locations.

Horton infiltration

The Horton infiltration is calibrated to improve the surface water levels. The top left plot in Figure 5.5 shows the observed and modelled surface water level upstream of Meetstuw. The modelled results show a large drop at the start due to the initialisation, followed by two peaks, while the observations show one larger buffered peak. Calibration is done between the infiltration ranges of clay and loamy sand. With the clay values (7.6 mm/h initial, 2.5 mm/h equilibrium), the water levels are too high. After two calibration steps, the final infiltration values are 12.05 mm/h (initial) and 3.15 mm/h (equilibrium). Key metrics are checked to see if the calibration improves the results, but they are not meaningful here because the response patterns of the model and the observations differ substantially. The focus is therefore on whether enough water is retained in the surface water domain. The results for the iteration steps are given in Appendix I.

Effective porosity

Next, the effective porosity is calibrated. First, the simulations with the low effective porosity of 0.1 and the high effective porosity of 0.35 are run. The groundwater levels that are located deeper (Schoolweg, Eimersweg and Camping) mostly show better key metric performances for the high effective porosity than for the low one, as shown in Appendix J. Conversely, the lower groundwater levels (Ten Barge and Meteoveld) perform better for the lower porosity compared to the higher porosity. Except when looking at R^2 for the groundwater Camping, Schoolweg and Eimersweg, this is the other way around, the key metric performs a bit better with the low effective porosity. Since the other metrics point all to the opposite, they are considered leading in the evaluation. For this reason, the method of a distributed approach is applied instead of a spatially lumped approach with uniform values. A raster is made of differing effective porosity values that are between 0.1 and 0.35. The values are based on the groundwater results for the base simulation where the value is 0.23, and the two extremes. Because of limited groundwater observations, all of the interpolation is based on estimation. The results for the final effective porosity raster is given in Figure 5.6. At all locations except Schoolweg and Eimersweg, the key metric performance after calibration is better than for the uniform high and low effective porosity cases. For Schoolweg and Eimersweg, the results are the same as for the high porosity case, since the final effective porosity at these locations is 0.35 for both.

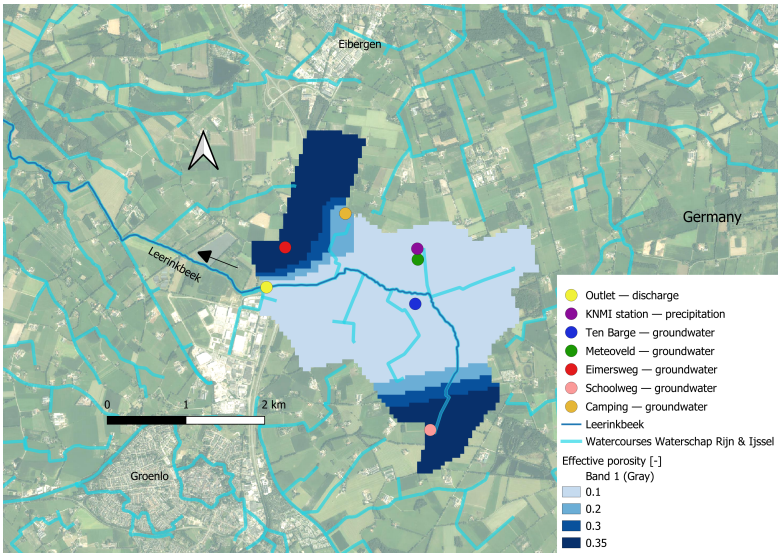

Figure 5.6: Study area with final effective porosity raster following the distributed approach after calibration.

Hydraulic conductivity

Lastly, the hydraulic conductivity is calibrated. The simulations with both high and low porosity are run. These values equal 10 and 0.1 m/d respectively. The results are given in Appendix K. First, the high hydraulic conductivity is analyzed. The surface water results highlight higher surface water level and higher delay compared to other simulations. Additionally, location Schoolweg, situated in the upstream part of the catchment, shows notable deviations between modelled and observed water levels, with the differences growing larger as the simulation progresses. There are also deviations in the other groundwater locations, but less extreme. In contrast to the high hydraulic conductivity, the lower hydraulic conductivity leads to better performance values except for the R^2 metric. It is investigated if the geometric mean between the two extremes, equal to 0.32 m/d, leads to better results. This is not the case, only Camping shows a bit better key performance results. While a higher hydraulic conductivity at this specific location would yield better results, applying the distributed approach by implementing a spatially varying raster for just one location is not feasible. The final parameter value of 0.1 m/d is selected, as the simulation results show no significant difference between 0.1 and 0.32 m/d. Therefore, further calibration is not necessary.

Final simulation

The final groundwater parameter values are based on the calibration results. Figure 5.7 shows the outcomes of the final calibration, and Table 5.1 lists the final parameter values. Compared to the base simulation in Figure 5.5, the amplitudes of the surface water levels are larger. Most key metrics for surface water improve, but they remain of limited value because the response pattern still differs substantially. In contrast, the key metrics for all groundwater locations show better performance than in the base simulation.

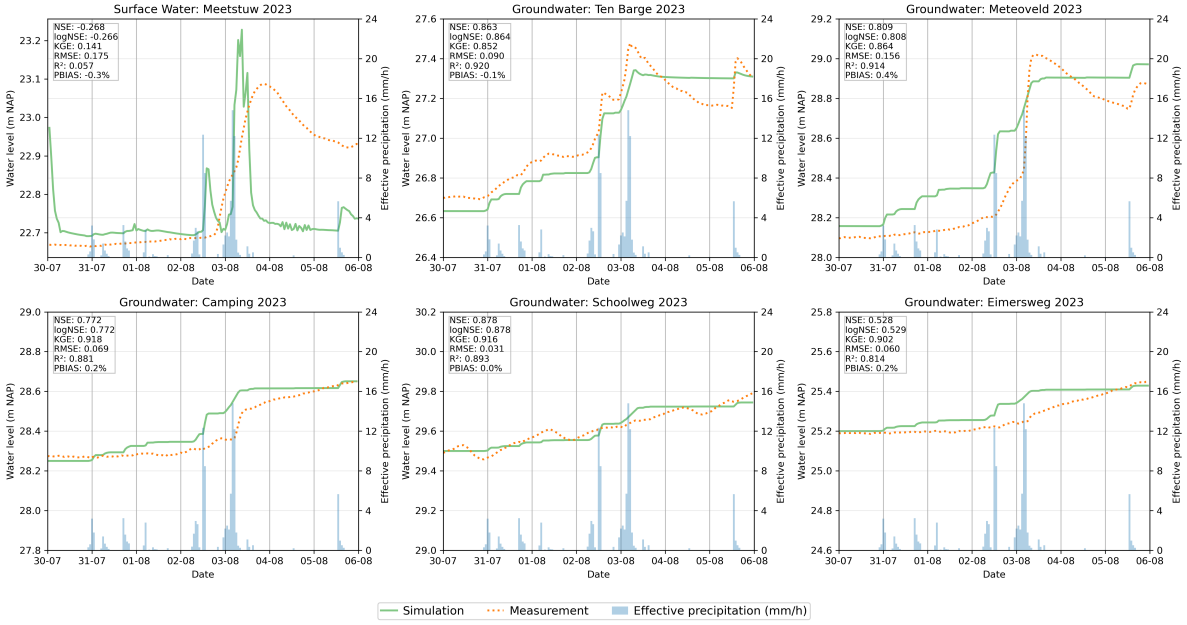

Figure 5.7: Final simulation with initial values. Upper left is surface water at Meetstuw, followed by the groundwater locations.

Groundwater settings in 3Di	Initial value	Final value	Unit
Impervious layer level	21.8	21.8	m NAP
Initial infiltration f_0	**610**	**289.2**	**mm/day**
Equilibrium infiltration f_{eq}	**122**	**75.6**	**mm/day**
Infiltration decay k	3	3	hours
Effective porosity ϕ_{eff}	**0.23**	**Raster**	**[-]**
Hydraulic conductivity K	**1.0**	**0.1**	**m/day**

Table 5.1: Final groundwater settings with calibrated settings in bold.

5.2.2. Calibration recharge

The final groundwater parameter values from the effective precipitation calibration serve as the initial parameters for the recharge calibration. Using these values, the model is simulated with recharge instead of effective precipitation, as shown in Figure 5.8.

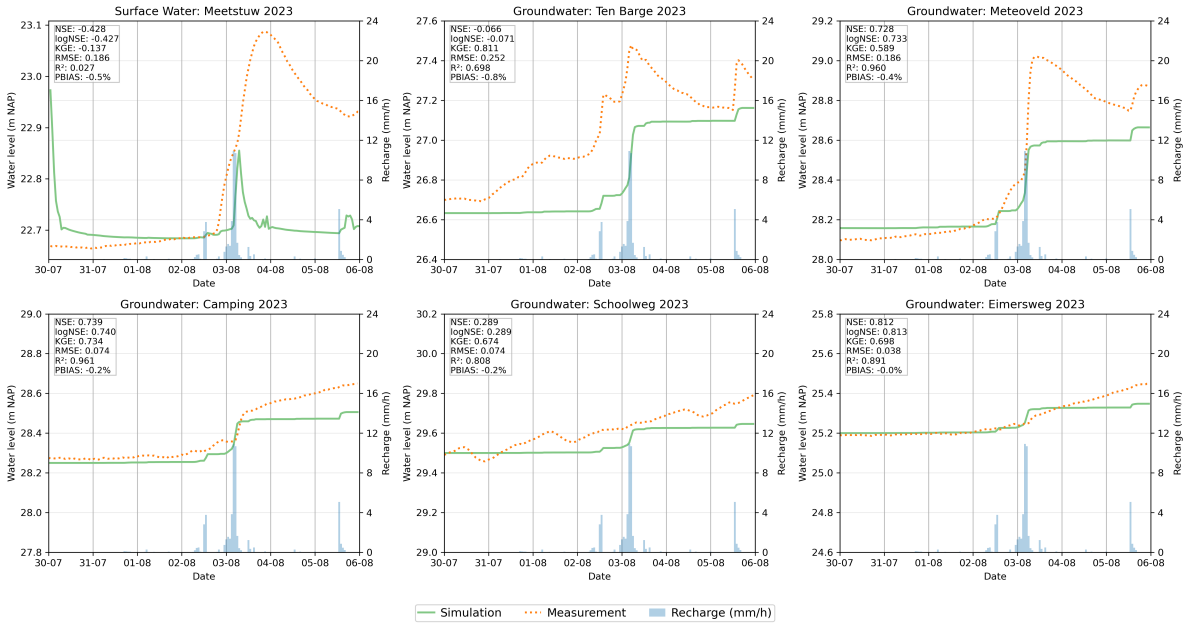

Figure 5.8: Calibration recharge 2023 base simulation.

Compared to the effective precipitation simulation, the results show a single peak instead of two. In addition, Figure 5.8 shows that the surface water level is too low, indicating that too little water is retained in the surface water domain. To improve this, the Horton based infiltration values are reduced to values corresponding to clay (7.6 mm/h initial, 2.5 mm/h equilibrium). The results are given in Figure 5.9.

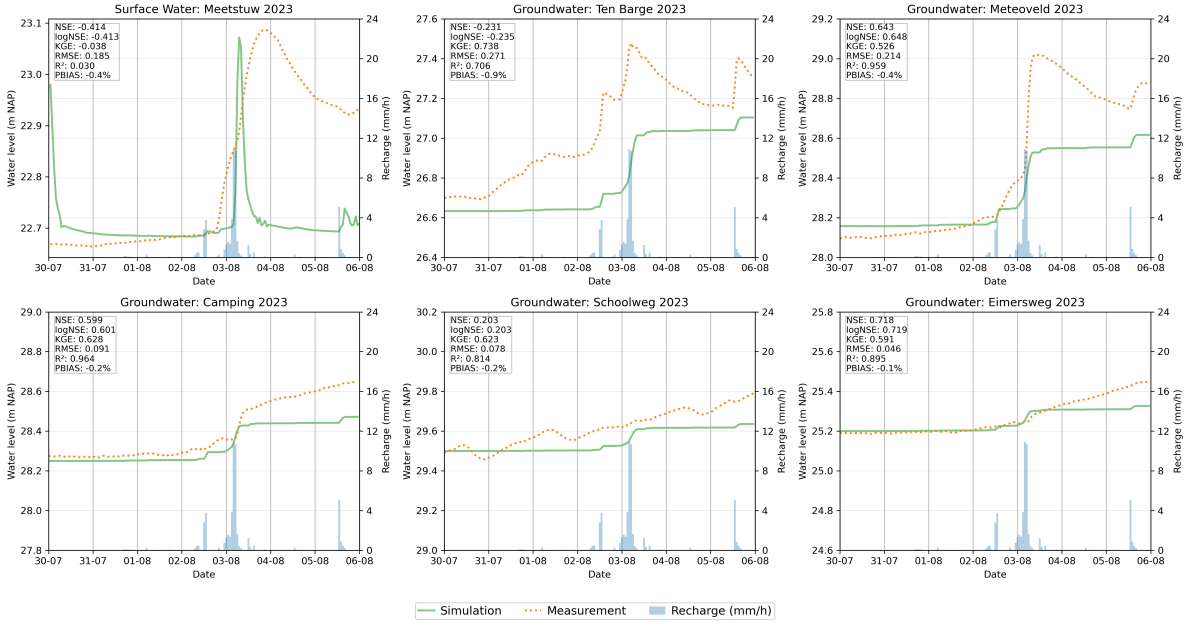

Figure 5.9: Calibration recharge 2023 final simulation.

Figure 5.9 shows that the calibration step raises the surface water level slightly. However, this comes at the expense of all groundwater locations, which perform worse than in the base simulation shown in Figure 5.8. Further calibration for groundwater is not done, because the groundwater domain already lacks water and this would require unrealistic parameter values.

5.2.3. Validation effective precipitation

This subsection presents the validation of the model by simulating the events of 2020 and 2015 with the same parameters that follow from the final groundwater parameters values. The difference with the previous simulations is that the effective precipitations are now simulated as input for the weeks of 2020 and 2015. Furthermore, the initial groundwater level rasters differ from each other, depending on the measurements.

Validation effective precipitation year 2020

The validation results for the event of 2020 are shown in Figure 5.10. The modelled surface water levels are higher than the observations. Additionally, there is no delay and buffer, as was with the event of 2023. For the groundwater measurements, different response patterns to the rain event are observed compared to the 2023 event. For instance, Meteoveld and Camping have more of a bulging effect compared to the event of 2023. In contrast, Ten Barge has a sharp spike increase followed by a decrease while the event of 2023 shows a gradual increase. The modelled groundwater results reveal similar patterns: instant increase followed by smaller step increases. Although the 2023 event provided reliable groundwater measurements, the 2020 results cannot be used to validate the model.

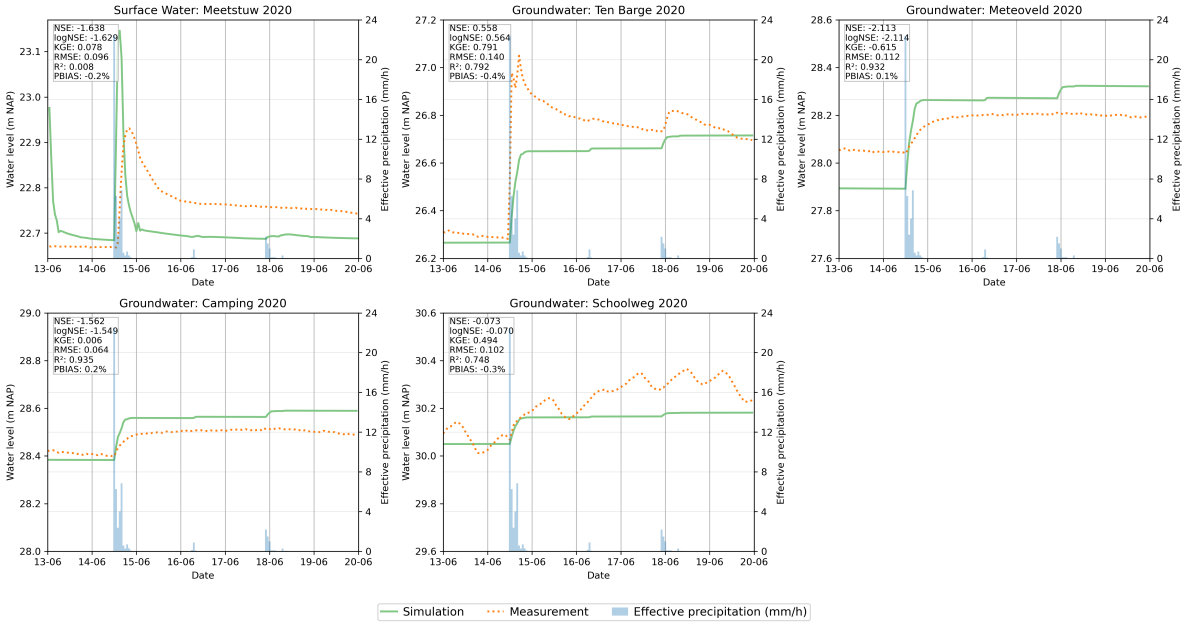

Figure 5.10: Validation effective precipitation for 2020 event.

Validation effective precipitation year 2015

Figure 5.11 presents the validation results for 2015. In contrast to the events of 2020 and 2023, the event of 2015 shows a much smaller surface water level response. At Meteoveld and Camping, the modelled groundwater levels have higher amplitudes than the observations. The groundwater levels also do not decrease after the peak. As with the 2020 event, the responses at Camping and Meteoveld are overestimated, and the initialisation at Meteoveld does not match the observations. Together with the 2020 event, this event shows that the model cannot be validated for peak flows after drought.

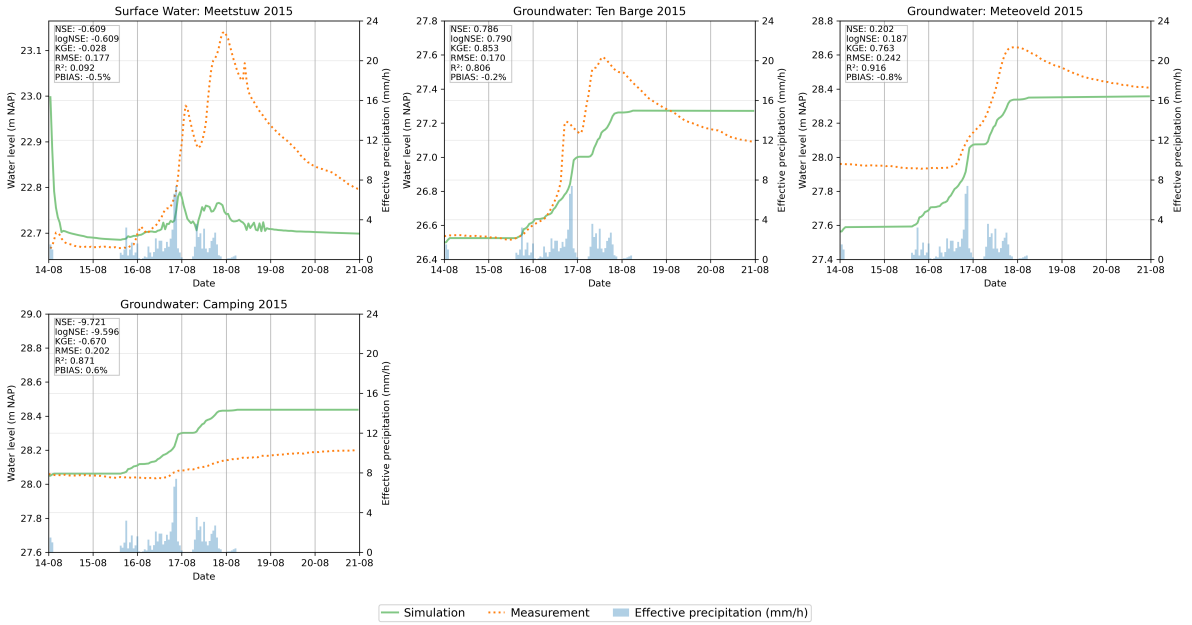

Figure 5.11: Validation effective precipitation for 2015 event.

5.2.4. Validation recharge

Following the Horton calibration for the event of 2023 with recharge input, the events of 2020 and 2015 are simulated with recharge with the same settings.

Validation recharge precipitation year 2020

The results for 2020 are given in Figure 5.12. The surface water plot illustrates that the surface water barely reacts to the input of the recharge. Also, the groundwater measurement locations indicate that the recharge is groundwater is too low, especially for Ten Barge.

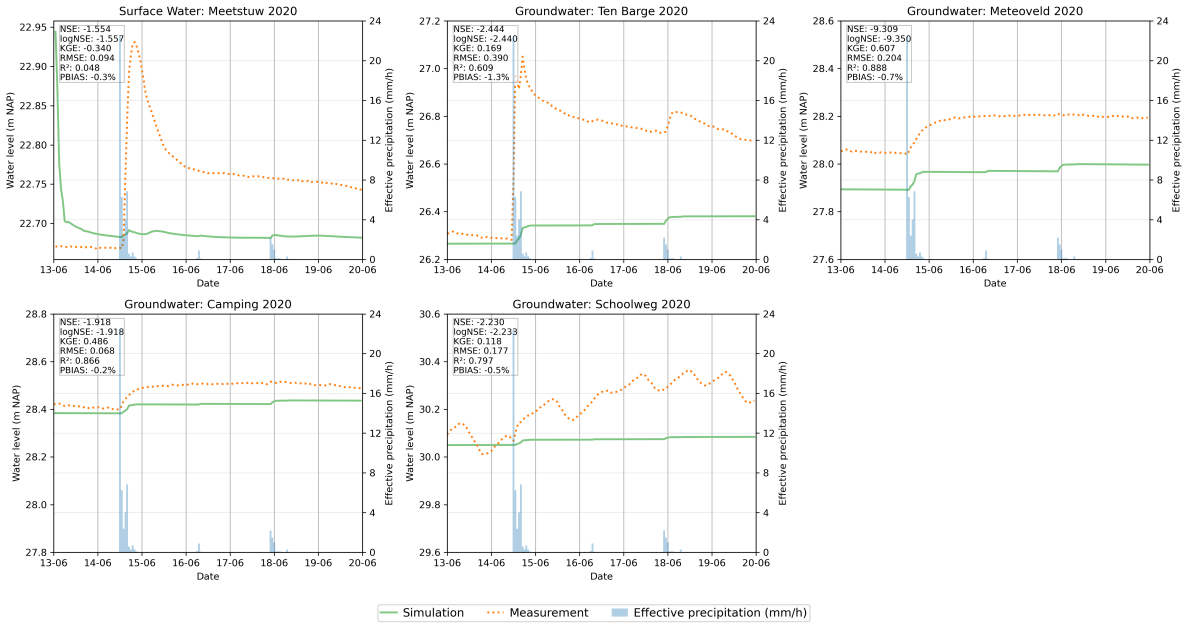

Figure 5.12: Validation recharge for 2020 event.

Validation recharge precipitation year 2015

The results for 2015 are given in Figure 5.13. For this event too, the surface plot barely reacts to the input of water. For Ten Barge and Meteoveld the groundwater recharge is on the low side. In contrast, the Camping site in Figure 5.13 shows better results when recharge is used as input compared to the final simulation with effective precipitation.

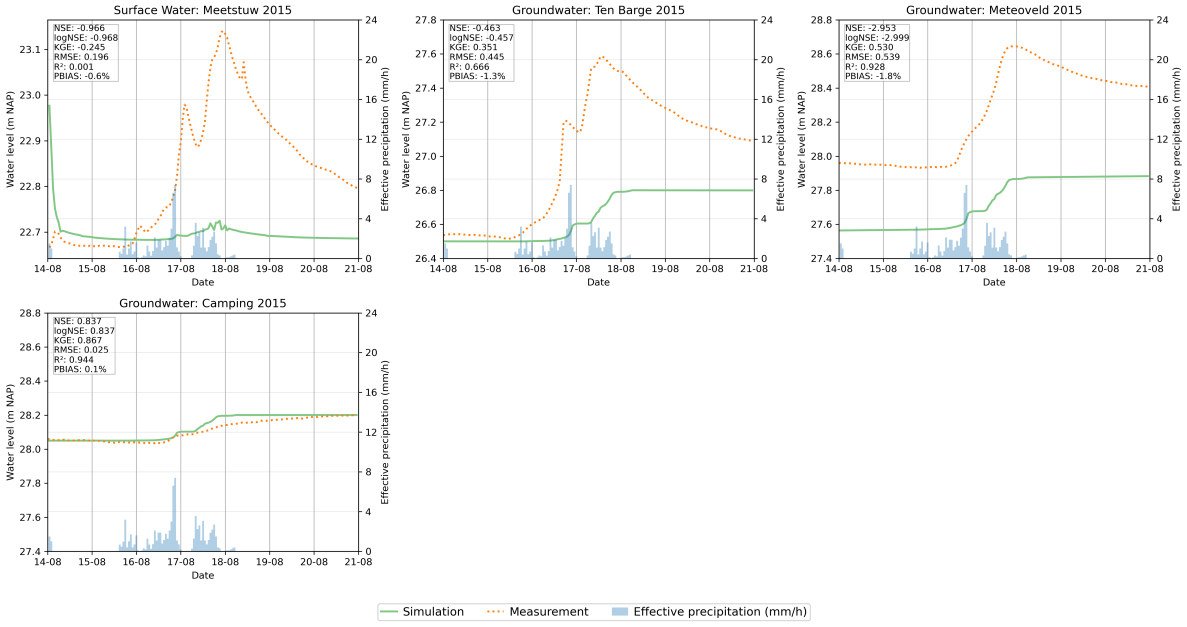

Figure 5.13: Validation recharge for 2015 event.

6

Discussion

This chapter discusses the results of this research. First, the findings from the data analysis are presented in Section 6.1. Thereafter, Section 6.2 elaborates on the 3Di model and its outcomes. The discussion first addresses the results for both effective precipitation and recharge. This is followed by subsections that highlight specific points and discuss the main limitations of the research. Lastly, Section 6.3 discusses if this case study can be generalized for other catchment systems.

6.1. Data analysis

First, Subsection 6.1.1 discusses the results of the SSI calculation and how methodological choices and criteria influenced them. Subsection 6.1.2 then examines the selected drought events and the criteria that shaped these outcomes. Finally, Subsection 6.1.3 presents the correlation analysis, with a particular focus on data uncertainty and validation.

6.1.1. SSI calculation

Within this study, the SSI is calculated from 1993 up to and including 2023. From the results, it is highlighted that at some points there is severe drought in which the SSI reaches -2. In recent years, the SSI remains below zero for longer periods. It is also observed that compared to older years, the years 2018, 2019 and 2022 depict a larger duration where the SSI remains below zero. The study by Altayeb (2023) reports only SSI-1 based on the GEV distribution for the period 2018-2024, which limits the comparison to these years. Apart from the missing values in the present dataset, the results appear relatively consistent with those of the study. A key difference is that Altayeb (2023) calculated SSI from simulated streamflow, whereas the present study relies on observed values. Consequently, the missing data in this study partly explains the discrepancies between the two series.

Beside the differences in data, methodological choices regarding the averaging timescale also influence the characterization of droughts. In this study, the 30-day averaging timescale (SSI-1) was applied. In comparison, Altayeb (2023) also examined 10-day and 90-day timescales for Hupsel in order to calculate SSI-actual and SSI-3 respectively. Among the tested distributions (Tweedie, Pearson Type III, Genlog and GEV), the results showed that GEV generally produced the lowest rejection rates, except for the 90-day average, where Genlog performed better. If the 90-day average would have been adopted for this study, the Genlog would have been the best fitted distribution, leading to different SSI calculation. Even though GEV was the best fit for the 10-day average as well, it still would have led to other results, which in turn could have required adjustments to the criteria for drought selection in the next step. Future research could explore the correlation analysis for shorter or longer droughts, using SSI-actual or SSI-3 respectively.

6.1.2. Selection of droughts

Using the chosen criteria, drought events with subsequent peak flows were extracted from the Hupsel time series. To obtain a larger set of results, the SSI threshold was adjusted from -1 to -0.5. This resulted in approximately 65 percent more events. Within literature, an SSI of around -0.5 is typically classified as a mild drought (Altayeb, 2023; Zalokar, Kobold, and Šraj, 2021; Wu et al., 2022). Given the hydrological conditions in the Netherlands, a threshold of -1 may be too stringent for the study area.

6.1.3. Correlation analysis

The correlation analysis produces clear results: run-off increases from the threshold of 0.22 mm^3/mm^3 onward, and seasonal patterns differ. The threshold represents the point at which the soil is close to saturation, leading to additional rainfall that cannot infiltrate and is instead routed to surface run-off. The relationship between antecedent soil moisture conditions and run-off is non-linear, with sharp increases once the threshold is exceeded. The event-based analysis highlights this threshold behaviour for individual peak events. When considering all droughts together, the correlation is stronger when comparing to only the droughts that have a soil water content larger than 0.22 mm^3/mm^3. However, this is mostly due to more outliers. Furthermore, the rolling-window analysis highlights how the relationship develops across different seasons. On the one hand, in winter, soils are generally wetter and evapotranspiration is low. On the other hand, in summer, drier conditions and higher evapotranspiration occur. Therefore in summer, the relationship between antecedent soil water content and peak flow is weaker, but the non-linear threshold behaviour is still clear once soils become saturated. Despite these consistent results, the accuracy of the soil water content data is uncertain. Therefore, it essential to address data uncertainty and validate the findings against other observations.

Data uncertainty

In the information document of Gleam (2024), there is no reporting of any uncertainties in the data that is based on satellite observations. In addition, the modelled data from GLEAM has a resolution of 0.1° by 0.1° latitude-longitude degrees. The Hupselse Beek lies within the resolution grid, but its area is approximately eleven times larger than that of the Hupselse Beek itself. While it is assumed that grid's water content data represents conditions in the whole Hupsel area, in reality it varies. The study of Rosenbaum et al. (2012) test site with an area of 0.27 km^2 in Wüstebach, Germany found that soil properties, topography, meteorological forcing, vegetation and groundwater drive spatial soil moisture patterns. The Hupsel study area also features varying soil properties (mainly loamy sand with a bit of peat and gravel), difference in groundwater flow, and modest elevation changes. These factors suggest that soil moisture conditions in the Hupsel catchment are more complex than what a coarse-resolution of 0.1° by 0.1° can represent.

Data validation

To validate the soil water content data, it is compared against in-situ measurements. "Droogte Zandgronden Nederland" is a project in which eleven sandy locations in The Netherlands including Hupsel measured soil moisture. The measurements were conducted at a 15 and 30 cm depth with sensors. The project was established to improve understanding of drought processes in sandy soil regions, with focus on the droughts of 2018 and 2019 (Heinen et al., 2023). The sensors are situated near the KNMI station. Since 2020, Droogteportaal Nederland (n.d.) has continued monitoring soil moisture at this site, with the data made publicly available. Although the overall flow is similar to the data from GLEAM, the extremes differ: the measurements display more pronounced highs and lows compared to GLEAM data. The absolute values of the measured soil moisture contents are not exact since the soil moisture sensors are not calibrated for the local soils (Heinen et al., 2023). It is therefore difficult to determine whether the deviations in extremes are due to the sensor itself or to GLEAM. Overall, the GLEAM data provide valuable insights in determining the effect of antecedent soil moisture conditions on run-off generation after hydrological drought.

6.2. 3Di

This study evaluates the 3Di model's performance for post-drought peak flows for both effective precipitation and recharge, forming Phase 3 of this research. The results are discussed first for effective precipitation in Subsection 6.2.1, followed by recharge in Subsection 6.2.2. The subsections first present the surface water results, then the groundwater results, and finally the water balance schematics. Thereafter, Subsection 6.2.3 highlights specific results of the distributed approach and Subsections 6.2.4 and 6.2.5 cover uncertainties and limitations.

6.2.1. Effective precipitation

Surface water

For the surface water, the 3Di results illustrate too responsive levels for all events. The peaks are too narrow and lacking any buffering effect. The observations highlight that there is not enough time for the system to empty, while for the 3Di model this is the case. The following are possible explanations that should be investigated in further 3Di modelling.

First, the surface water domain was not calibrated. The friction values in 3Di may be too low, as the creek is mostly assigned a Manning coefficient of 0.026, which may be too smooth for a lowland creek. In addition, all weirs are represented as obstacles with a single crest level through which water can pass, whereas in reality their geometry varies along the width, which could have influenced the surface water domain. Calibration of surface water parameters such as friction or a more detailed representation of obstacles could have helped reduce the overly strong response. Second, the data is limited: all groundwater stations are at the edges and mostly upstream of the Hupsel, and surface water is only measured at the most downstream location point. This makes it difficult to quantify groundwater flow to the creek and to initialize water levels accurately. A third point is that the effective porosity near the creek may be too high. Lowering this value during calibration gave more delay and buffering in the surface water response. The values were not reduced further to stay within realistic ranges. However, past drought conditions may have reduced the effective porosity even more, and its variation during the week could also play a role. A fourth explanation for the too responsive surface water could be that some system dynamics are missing in the model. Small weirs are present in the area, but their actual operation is not well known, and parts of the catchment have pipe drainage (G. Roelofs, Waterschap Rijn & Ijssel, personal communication, September 2025). This was not included in the model. Finally, a fifth explanation could be that 3Di does not simulate the unsaturated zone, which means infiltration delays and subsurface storage are missing. This can make the modelled response more peaked, although with this research this alone cannot explain the mismatch during drought events.

Groundwater

The groundwater results show relatively good key-metric performance for the 2023 event. The results show a noticeable difference between Ten Barge and Meteoveld compared to the other three locations, with Ten Barge and Meteoveld having lower recharge. However, the drop in groundwater levels at Ten Barge and Meteoveld towards the end of the simulation is not reproduced. This can be attributed to the absence of a groundwater boundary condition in the model. Compared with the 2023 event, the validation events show poorer performance. In some cases the model initialization is insufficient, leading to a response that is either too low (e.g., Ten Barge 2020) or too high (e.g., Camping 2015). The observations also reveal different response patterns: in 2020, Ten Barge and Meteoveld respond differently to effective precipitation, while in 2015 and 2023 their responses are more alike. At Camping, the 2015 event shows only limited recharge, whereas the 2020 event displays a more pronounced bulging effect. This means that for groundwater, there are some dynamics that the model fails to capture. In addition, incorporating data on groundwater inflows and outflows across the model boundaries could have improved the simulated decline in groundwater levels following the peak caused by extreme precipitation.

Water balance

Figure 6.1 illustrates the water balance for both the base simulation as well as the simulation with the final calibrated parameters. For each case, rainfall and boundary outflow over the one-week simulation are shown outside the box. Their difference represents the net input, which is distributed across the groundwater, surface water, and 1D network domains. Inside the boxes, storage changes are reported as the difference between the end and the beginning of the simulation period. In the groundwater domain, storage change comes from the balance between infiltration (downward flux) and exfiltration (upward flux), with exfiltration shown as negative in 3Di. The comparison shows that calibration changes both the outflow at the boundaries and how storage is divided between the domains.

In both simulations, most effective precipitation ends up in the groundwater domain. However, the distribution shifts in the final simulation. Surface water storage increases (from -5271 m^3 to +1332 m^3), showing some success in retaining water at the surface. However, this is outweighed by a strong rise in boundary outflow (from 33,811 m^3 to 123,806 m^3), meaning water still leaves the system too quickly. Consequently, groundwater storage decreases by nearly 100,000 m^3 and overall retention decreases

to about 90,000 m^3 compared to the base simulation. Although surface water storage increases, the changes cause faster drainage instead of more retention. The intermediate water balance steps are shown in Appendix I, Appendix J, and Appendix K. These steps show that the reduction in Horton infiltration is the main cause of the faster outflow. This underlines that additional calibration in the surface water domain is needed to reduce fast drainage.

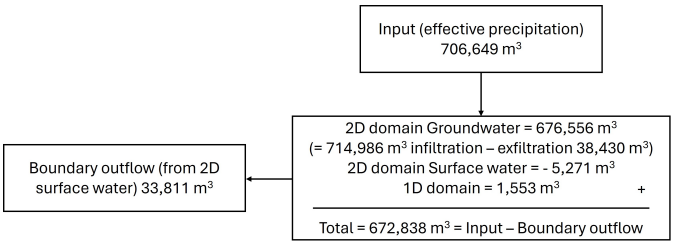

(a) Base simulation

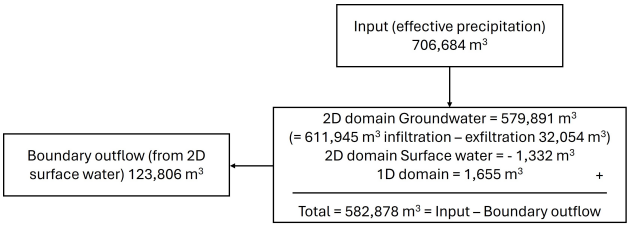

(b) Final calibration

Figure 6.1: Water balance schematics for the base (a) and calibrated (b) simulations for effective precipitation P_E. All fluxes are given in m^3 over the one-week simulation period.

6.2.2. Recharge

Surface water

The same parameter values were used as those obtained from the calibration with effective precipitation as the initial starting point for the simulation with recharge. The first step was tuning the Horton infiltration for the calibration event. When using recharge as input for 3Di, compensation was needed through smaller Horton infiltration values in order for the surface water levels to match observations, with values representative of clay applied to adjust the levels. This adjustment successfully raised the simulated surface water levels to the observed range. However, similar to the simulations with effective precipitation, the modelled results for the 2023 event still showed a flashy response without buffering. One difference between the recharge and effective precipitation runs is that the recharge case produced a single peak instead of two. Including soil moisture conditions could have influenced this result, but since the surface water performance is poor, no clear conclusion can be drawn. No further calibration steps for Horton infiltration were performed, in order to retain realistic parameter values for the Hupsel.

Groundwater

In the initial simulations, groundwater levels were already not well reproduced. After the calibration step, when infiltration values were lowered further, the amount of recharge to groundwater decreased and the results became even less accurate. This undermines the justification for decreasing Horton infiltration, since it came at the expense of an even poorer groundwater performance. Further calibration of effective porosity and hydraulic conductivity was not considered, as this would have led to unrealistic values for the Hupsel.

Water balance

Figure 6.2 illustrates the water balance for both the base simulation as well as the simulation after the calibration step. The same patterns is seen as with effective precipitation. When infiltration decreases, more water remains in the surface water domain, but the boundary outflow shows that it leaves the system more quickly.

In 3Di, Horton based infiltration is used to add a delay in the transfer of water from the surface to the groundwater domain, thereby mimicking the unsaturated zone. Combining 3Di with a bucket model could create overlap in representing the same processes. It is possible to turn off Horton infiltration by setting very high values, but then all water would flow directly to groundwater instead of being retained in the surface water. Therefore, further research is needed to assess the effect of not representing soil moisture conditions in 3Di for peak events following droughts.

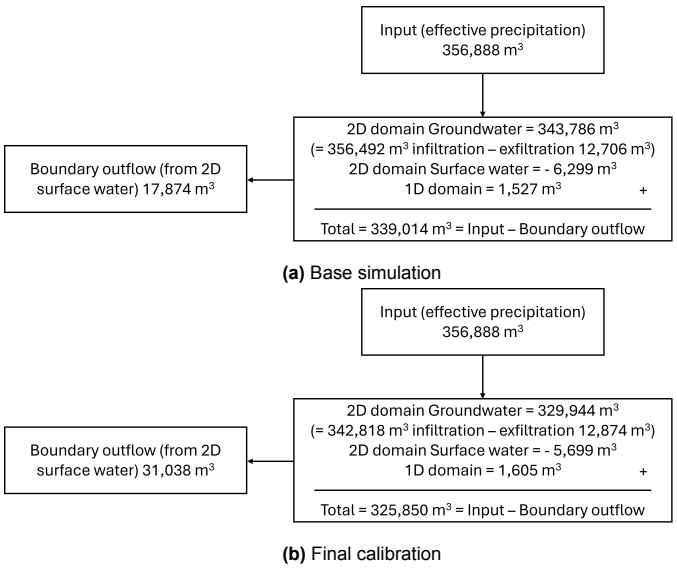

Figure 6.2: Water balance schematics for the base (a) and calibrated (b) simulations for recharge R. All fluxes are given in m^3 over the one-week simulation period.

6.2.3. Groundwater response

Groundwater observations show that locations respond differently to rainfall. Meteoveld and Ten Barge exhibit stronger and faster responses, while Camping, Schoolweg, and Eimersweg respond more gradually. These differences reflect specific characteristics of the study area and indicate how they should be represented in further 3Di modelling. To account for these differences, the distributed approach uses varying effective porosity values. Relatively higher values fit better for Camping, Eimersweg, and Schoolweg, while lower values fit better for Meteoveld and Ten Barge. This adjustment improves the representation of dynamic responses. Higher effective porosity means greater buffering capacity, leading to smaller groundwater fluctuations after rainfall. In contrast, lower values imply reduced storage and therefore stronger fluctuations under the same effective precipitation or recharge input.

Literature suggests that this distinction is also related to soil type, with higher effective porosities typically found in sandy soils due to their greater connected pore space, and lower values in silt- and clay-rich soils (Urumović and Urumović Sr., 2016), as also discussed in subsection 4.3.1. It is discussed whether differences in soil type around the area can justify the differences in effective porosity.

Figure 6.3 illustrates the study area with the profile defined by BOFEK2020, accessed via Waterschap Rijn & Ijssel. It is seen that apart from the differences of “weak” or “strong” there is not such a strong difference in soil type. The “strong” would refer to more sand content, while “weak” more silt/clay content. It is seen that Schoolweg is in the same category of soil category compared to Ten Barge and Meteoveld (weak loamy sandy soils I), even though Schoolweg shows such different response to groundwater recharge compared to Ten Barge and Meteoveld. Additionally, Camping is also located in a weaky loamy sandy soil, despite the expectation that the site would consist of stronger sandy material.

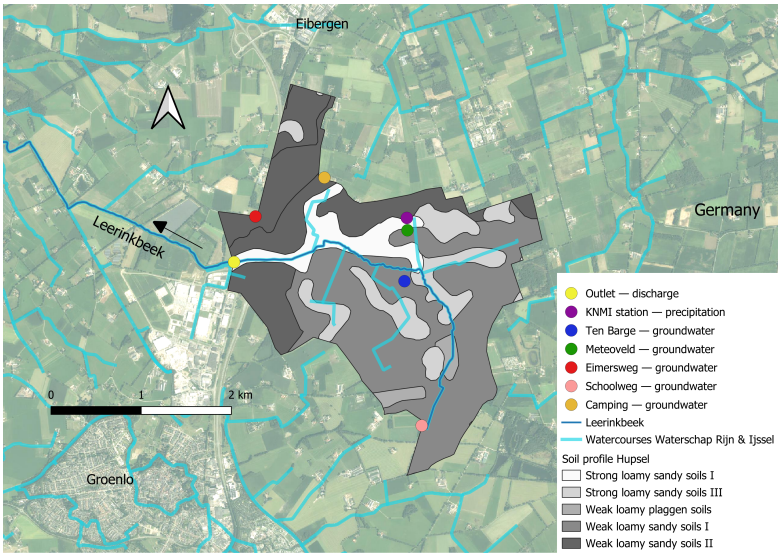

Figure 6.3: Soil profile of research area. Roman numerals distinguish soil variants within this type. Aerial image obtained from the WMS service Actueel Ortho25 with a resolution of 25 cm is used to map the background. Water courses are illustrated with lines and measurement points with dots.

This means the difference in effective porosity compensating for the different groundwater responses cannot be justified by a clear difference in soil composition. The filter depths of the monitoring wells are comparable (G. Roelofs, Waterschap Rijn & Ijssel, personal communication, June 2025). Therefore the measurements are likely from the same aquifer. The remaining explanation lies in differences in the hydrological setting. Ten Barge and Meteoveld are situated in areas with more seepage and intensive draining (G. Roelofs, Waterschap Rijn & Ijssel, personal communication, June 2025). As a result, less storage is available to buffer recharge, which causes stronger groundwater fluctuations. In addition, the antecedent conditions of the soil plays a role. Prolonged dry periods or differences in the initial dryness of the unsaturated zone can affect which pores are active, which helps explain some of the observed differences. This indicates that effective porosity in the model is not only representing soil physical properties, but also compensating for differences in drainage intensity, groundwater regime, and antecedent conditions.

In 3Di, it is possible to compensate for these processes by adjusting effective porosity. For the event of 2023, this worked reasonably well. However, for the other years the performance of the simulations reduced. For instance, at Meteoveld the modelled response was too strong for years 2015 and 2020. To better capture the differing responses, model improvements should focus on including leakage and groundwater boundary conditions. While it is acceptable to adjust effective porosity within a plausible range, event-based evaluation is needed to determine which processes (drainage, seepage, storage) are dominant in controlling groundwater fluctuations.

6.2.4. Input

In order to simulate peak discharge after drought, time series for both effective precipitation as well as lateral recharge was needed as input. Rainfall was available via KNMI on hourly basis, the time step goal for the output of simulation. Therefore, the modelled actual evaporation, available from GLEAM on a daily basis, had to be scaled. Since radiation was measured on hourly basis, it was decided to scale the modelled actual evaporation based on this radiation. This is a large assumption since it would mean no evaporation at night. In addition, for both effective precipitation and recharge, interception was included in the calculations. However, the effect of varying $S_{I,\text{max}}$ was not considered and should be investigated within further research.

6.2.5. Calibrations

For modelling the Hupselse Beek, a minimum cell size of 10 m by 10 m was chosen with three grid cell levels for grid refinement. The cell size was chosen to be as accurate as possible without enlarging the computational time too much. When including the effective porosity raster, this time equaled to around one hour and 15 minutes. Calibration for different cell sizes and grid refinement based on an ensemble analysis could have strengthened the results.

6.3. Generalization of the case study

There are several factors that are characteristic for the Hupsel. The area has shallow groundwater conditions, a mildly sloping surface, and heterogeneous soil compositions (mainly loamy sand, with a bit of clay, gravel, and peat). Another distinctive feature is the strong variation in groundwater level measurements with depth, which required calibration of effective porosity across a wider range of values. Despite being a relatively small brook system, the Hupsel exhibits internal variability. This heterogeneity likely contributed to the responsiveness of the system when modelling with 3Di. For instance, the relatively rapid reaction of surface water may be linked to the slope and groundwater dynamics. By contrast, a system with more uniform groundwater conditions, a flatter topography, and more homogeneous soil characteristics could be expected to produce different results. However, this requires further research. The characteristics of the Hupsel therefore suggest that insights from this study may be generalized to other lowland catchments with shallow groundwater and gentle slopes.

7

Conclusion

The goal of this case study research is to answer the following questions:

1. How do antecedent soil moisture conditions during a hydrological drought correlate with peak discharge during subsequent extreme rainfall events?

2. How does 3Di perform in simulating peak flow events after drought conditions when using effective precipitation as input?

3. How does incorporating soil moisture conditions through the unsaturated zone affect the simulation of peak discharge event after hydrological drought in the 3Di model?

For the Hupselse Beek, a positive correlation is observed between soil water content (as an indicator of relative soil moisture) during drought and run-off after drought. This relationship is evident when comparing antecedent soil moisture levels five days prior to the most extreme peak discharges. Seasonal variation affects the strength and pattern of this correlation. A clear threshold in soil water content is observed around 0.22 mm^3/mm^3. Below this threshold, drought events predominantly occur during summer or transitional seasons. Once this threshold is exceeded, winter conditions and non-drought events appear, with run-off ratios increasing accordingly. The correlation coefficient is assessed with the total data as well as the data that is higher than the threshold. The results for this are 0.66 and 0.56 respectively. This case study supports the observation that, during hydrological drought, the relationship between antecedent soil moisture conditions and run-off is non-linear. For the soils in the Hupselse Beek catchment, there is no indication that extremely dry conditions lead to soil hydrophobicity that would cause deviations from this non-linear pattern. This suggests that run-off generation in this catchment remains responsive to soil moisture, even under hydrological drought conditions.

The effective precipitation for three chosen drought events is simulated in the 3Di model. Across all events, the surface water reacts too quickly and produces sharp peaks that do not match the buffered observations. Several aspects could help improve the surface water response, one of the main ones being calibration of the surface water domain, for example by adjusting friction values. In contrast, the estimated ranges of groundwater recharge are relatively accurate, especially for the 2023 event. For the 2020 and 2015 events, the fit is weaker, which may be related to initialization and the lack of boundary conditions. Including soil moisture conditions in 3Di reduces the hourly input compared to effective precipitation. To match measured surface water levels under this setup, Horton infiltration needs to be decreased, but this produces narrow spikes and further reduces groundwater recharge. In this case, using the bucket model as input does not improve performance and in fact leads to poorer results. Moreover, the imperfect outcomes for effective precipitation cannot be attributed solely to the absence of an unsaturated zone in 3Di, since infiltration is already represented through Horton. To conclude, the current model struggles to reproduce surface water dynamics, which shows the need for calibration of the surface water domain. The groundwater domain, however, performs relatively well and shows strong potential for 3Di in modelling peak flows after hydrological drought.

8

Recommendations

This thesis closes with two sets of recommendations. Recommendations for future research are provided in Section 8.1, and recommendations for Nelen & Schuurmans in Section 8.2.

8.1. Recommendation for future research

The outcomes of this study point to several directions for future research. One important aspect concerns methodological choices, such as the averaging timescale used for drought characterization. This study applied a 30-day averaging timescale (SSI-1), but shorter (e.g., 10-day) or longer (e.g., 90-day) timescales can yield different outcomes and even affect the choice of statistical distribution for SSI calculation. Exploring such variations in future research could help make drought analysis and correlation studies more reliable.

Chapter 1 explains that there is a knowledge gap in the interaction between peak flow, drought, and the hydrological processes that play a role. This research focused on soil moisture, but other processes, such as vegetation, are also relevant. Furthermore, for peak flow after drought events, it would be worth studying how long it takes for soil moisture to recover to pre-drought levels, which could provide meaningful insights into drought recovery.

8.2. Recommendation for Nelen & Schuurmans

In 3Di, the interaction between surface water and groundwater domains is crucial. Surface water infiltration determines how much recharge enters the groundwater, while shallow groundwater levels can lead to exfiltration that feeds the surface water. To capture these dynamics, calibration and initialization must consider both domains together. Reliable modelling therefore requires detailed information about the study area, including initial water levels and boundary conditions.

For calibration, it is recommended to start with the surface water domain. An important aspect here is to include the friction raster, since the current results suggest that the modelled system responds too quickly. Adjusting these values could slow down the response. After the surface water calibration, the groundwater domain can be added, and its interaction with the surface water domain can then be examined. This stepwise approach supports consistent calibration of both domains and can therefore contribute to drought modelling within 3Di.

References

Altayeb, Maab (2023). *Standardized Streamflow Index for Streamflow Drought: Development of New Functionality in the Dutch Drought Portal*. Unpublished MSc internship report. Provided by Prof. [C. Brauer], not publicly available.

Ankum, P. (2002). *Design of open-channels and hydraulic structures*. Study material CT3410, TU Delft.

Berg, A. and J. Sheffield (2018). "Climate Change and Drought: the Soil Moisture Perspective". In: *Curr Clim Change Rep* 4, pp. 180–191. DOI: 10.1007/s40641-018-0095-0.

Bodí, Merche B., Isabel Muñoz-Santa, Carmen Armero, Stefan H. Doerr, Jorge Mataix-Solera, and Artemi Cerdà (2013). "Spatial and temporal variations of water repellency and probability of its occurrence in calcareous Mediterranean rangeland soils affected by fires". In: *CATENA* 108. Soil Water Repellency, pp. 14–25. ISSN: 0341-8162. DOI: https://doi.org/10.1016/j.catena.2012.04.002. URL: https://www.sciencedirect.com/science/article/pii/S034181621200077X.

Brauer, C. C., Y. van der Velde, A. J. Teuling, and R. Uijlenhoet (2018). "The Hupsel Brook catchment: Insights from five decades of lowland observations". In: *Vadose Zone Journal* 17.1, pp. 1–8. DOI: 10.2136/vzj2018.03.0056.

Brunner, Manuela I., Louise Slater, Lena M. Tallaksen, and Martyn Clark (2021). "Challenges in modeling and predicting floods and droughts: A review". In: *WIREs Water* 8.3, e1520. DOI: 10.1002/wat2.1520. URL: https://doi.org/10.1002/wat2.1520.

Chen, Yi-Feng, Xiao-Ming Ling, Ming-Ming Liu, Ran Hu, and Zhibing Yang (2018). "Statistical distribution of hydraulic conductivity of rocks in deep-incised valleys, Southwest China". In: *Journal of Hydrology* 566, pp. 216–226. ISSN: 0022-1694. DOI: https://doi.org/10.1016/j.jhydrol.2018.09.016. URL: https://www.sciencedirect.com/science/article/pii/S0022169418307029.

Dekker, Louis W. and Coen J. Ritsema (1996). "Variation in water content and wetting patterns in Dutch water repellent peaty clay and clayey peat soils". In: *CATENA* 28.1, pp. 89–105. ISSN: 0341-8162. DOI: https://doi.org/10.1016/S0341-8162(96)00047-1. URL: https://www.sciencedirect.com/science/article/pii/S0341816296000471.

Droogteportaal Nederland (n.d.). *Droogteportaal*. https://www.droogteportaal.nl/.

Espinoza, Eduardo Acuña, Ralf Loritz, Manuel Álvarez Chaves, Nicole Bäuerle, and Uwe Ehret (2024). "To bucket or not to bucket? Analyzing the performance and interpretability of hybrid hydrological models with dynamic parameterization". In: *Hydrology and Earth System Sciences* 28.12, pp. 2705–2719. DOI: 10.5194/hess-28-2705-2024. URL: https://hess.copernicus.org/articles/28/2705/2024/.

Farrick, Kegan K. and Brian A. Branfireun (2014). "Soil water storage, rainfall and runoff relationships in a tropical dry forest catchment". In: *Water Resources Research* 50.12, pp. 9236–9250. DOI: https://doi.org/10.1002/2014WR016045. URL: https://agupubs.onlinelibrary.wiley.com/doi/abs/10.1002/2014WR016045.

Gilliom, Ryan, Bell, Hogue, and John Mccray (Oct. 2019). "A Rainwater Harvesting Accounting Tool for Water Supply Availability in Colorado". In: *Water* 11, p. 2205. DOI: 10.3390/w11112205.

Gleam (2024). *README: Documentation for [GLEAM4.2 Datasets]*. Included with downloaded dataset. Available after download; not publicly accessible online.

Heinen, Marius, Jos van Dam, Ruud Bartholomeus, Janine de Wit, Gé van den Eertwegh, and Mirjam Hack-ten Broeke (2023). *Droogtemonitoring: Vergelijking metingen bodemvochtgehaltes met SWAP-WOFOST simulaties*. Tech. rep. Version V04, June 2023. KLIMAP / Wageningen Environmental Research. URL: https://klimap.nl/images/Proefgebieden/KLIMAP_droogtemonitoring_V04_20230613.pdf.

IPCC (2023). *Climate change 2023: Synthesis report*. Ed. by Core Writing Team, H. Lee, and J. Romero. IPCC, pp. 35–115. DOI: 10.59327/IPCC/AR6-9789291691647.

Koninklijk Nederlands Meteorologisch Instituut (n.d.). *Automatische weerstations*. URL: https://www.knmi.nl/kennis-en-datacentrum/uitleg/automatische-weerstations.

Lee, D. M., W. D. Reynolds, D. E. Elrick, and B. E. Clothier (1985). "A Comparison of Three Field Methods for Measuring Saturated Hydraulic Conductivity". In: *Canadian Journal of Soil Science* 65. Received 8 Jan. 1985; accepted 9 Apr. 1985, pp. 563–573.

Lucas-Borja, Manuel Esteban, Demetrio Antonio Zema, Pedro Antonio Plaza-Álvarez, Vesna Zupanc, Jantiene Baartman, Javier Sagra, Javier González-Romero, Daniel Moya, and Jorge de las Heras (2019). "Effects of Different Land Uses (Abandoned Farmland, Intensive Agriculture and Forest) on Soil Hydrological Properties in Southern Spain". In: *Water* 11.3. ISSN: 2073-4441. URL: https://www.mdpi.com/2073-4441/11/3/503.

Matanó, A., R. Hamed, M. I. Brunner, M. H. Barendrecht, and A. F. Van Loon (2025). "Drought decreases annual streamflow response to precipitation, especially in arid regions". In: *Hydrology and Earth System Sciences* 29, pp. 2749–2764. DOI: 10.5194/hess-29-2749-2025. URL: https://doi.org/10.5194/hess-29-2749-2025.

Muñoz-Castro, Eduardo, Bailey J. Anderson, Paul C. Astagneau, Daniel L. Swain, Pablo A. Mendoza, and Manuela I. Brunner (2025). "How well do hydrological models simulate streamflow extremes and drought-to-flood transitions?" In: *EGUsphere*. Preprint. Discussion started: 24 March 2025. CC BY 4.0 License. DOI: 10.5194/egusphere-2025-781. URL: https://doi.org/10.5194/egusphere-2025-781.

Nelen & Schuurmans (2025). *3Di Documentation*. URL: https://docs.3di.live/index.html#.

Nelen & Schuurmans (n.d.). *About us - 3Di*. URL: https://3diwatermanagement.com/about-us/.

Pizzorni, M., A. Innocenti, and N. Tollin (2024). "Droughts and floods in a changing climate and implications for multi-hazard urban planning: A review". In: *City and Environment Interactions* 24, p. 100169. DOI: 10.1016/j.cacint.2024.100169.

Prudic, David E. (1991). *Estimates of Hydraulic Conductivity from Aquifer-Test Analyses and Specific-Capacity Data, Gulf Coast Regional Aquifer Systems, South-Central United States*. Water-Resources Investigations Report 90-4121. Austin, Texas: U.S. Geological Survey.

Rosenbaum, U., H. R. Bogena, M. Herbst, J. A. Huisman, T. J. Peterson, A. Weuthen, A. W. Western, and H. Vereecken (Oct. 2012). "Seasonal and event dynamics of spatial soil moisture patterns at the small catchment scale". en. In: *Water Resources Research* 48.10, W10544. ISSN: 0043-1397, 1944-7973. DOI: 10.1029/2011WR011518. URL: https://onlinelibrary.wiley.com/doi/10.1029/2011WR011518.

Saksena, Siddharth, Venkatesh Merwade, and Peter J. Singhofen (2019). "Flood inundation modeling and mapping by integrating surface and subsurface hydrology with river hydrodynamics". In: *Journal of Hydrology* 575, pp. 1155–1177. ISSN: 0022-1694. DOI: https://doi.org/10.1016/j.jhydrol.2019.06.024. URL: https://www.sciencedirect.com/science/article/pii/S0022169419305657.

Schoener, Gerhard and Mark C. Stone (2019). “Impact of antecedent soil moisture on runoff from a semiarid catchment”. In: *Journal of Hydrology* 569, pp. 627–636. ISSN: 0022-1694. DOI: https://doi.org/10.1016/j.jhydrol.2018.12.025. URL: https://www.sciencedirect.com/science/article/pii/S0022169418309740.

TNO – Geological Survey of the Netherlands (n.d.[a]). *Boxtel Formation*. In *Stratigraphic Nomenclature of the Netherlands*. Last reviewed 2019. URL: https://www.dinoloket.nl/en/stratigraphic-nomenclature/boxtel-formation.

TNO – Geological Survey of the Netherlands (n.d.[b]). *Breda Formation*. In *Stratigraphic Nomenclature of the Netherlands*. Last reviewed 2019. URL: https://www.dinoloket.nl/en/stratigraphic-nomenclature/breda-formation.

TNO – Geological Survey of the Netherlands (n.d.[c]). *DINOloket: BRO REGIS II v2.2.3 – Ondergrondmodellen*. URL: https://www.dinoloket.nl/ondergrondmodellen/kaart.

TNO – Geological Survey of the Netherlands (n.d.[d]). *Sterksel Formation*. In *Stratigraphic Nomenclature of the Netherlands*. Last reviewed 2019. URL: https://www.dinoloket.nl/en/stratigraphic-nomenclature/sterksel-formation.

Urumović, K. and K. Urumović Sr. (2016). “The referential grain size and effective porosity in the Kozeny–Carman model”. In: *Hydrology and Earth System Sciences* 20.5, pp. 1669–1680. DOI: 10.5194/hess-20-1669-2016. URL: https://hess.copernicus.org/articles/20/1669/2016/.

Van Loon, A. F. (2013). “On the propagation of drought. How climate and catchment characteristics influence hydrological drought development and recovery”. PhD thesis. Wageningen University.

Van Loon, A. F. (2015). “Hydrological drought explained”. In: *WIREs Water* 2.4, pp. 359–392. DOI: 10.1002/wat2.1085.

Van Loon, A. F. et al. (2016). “Drought in a human-modified world: Reframing drought definitions, understanding, and analysis approaches”. In: *Hydrology and Earth System Sciences* 20.9, pp. 3631–3650. DOI: 10.5194/hess-20-3631-2016.

Volp, N. D., B.C. van Prooijen, and G.S. Stelling (2013). “A finite volume approach for shallow water flow accounting for high-resolution bathymetry and roughness data”. In: *Water Resources Research* 49.7, pp. 4126–4135. DOI: https://doi.org/10.1002/wrcr.20324.

Volp, Nicolette (2025). *Advanced Module Groundwater Modelling*. Lecture slides, 3Di Training. Presented at Nelen & Schuurmans.

Wu, Jiefeng, Huaxia Yao, Xiaohong Chen, Gaoxu Wang, Xiaoyan Bai, and Dejian Zhang (2022). “A framework for assessing compound drought events from a drought propagation perspective”. In: *Journal of Hydrology* 604, p. 127228. ISSN: 0022-1694. DOI: https://doi.org/10.1016/j.jhydrol.2021.127228. URL: https://www.sciencedirect.com/science/article/pii/S0022169421012786.

Xu, Zixuan, Jinfeng Ma, Hua Zheng, Lijing Wang, Lingxiao Ying, Ruonan Li, and Yanzheng Yang (2024). “Quantification of the flood mitigation ecosystem service by coupling hydrological and hydrodynamic models”. In: *Ecosystem Services* 68, p. 101640. ISSN: 2212-0416. DOI: https://doi.org/10.1016/j.ecoser.2024.101640. URL: https://www.sciencedirect.com/science/article/pii/S2212041624000470.

Ye, Sheng, Lin Liu, Jiyu Li, Hailong Pan, Wei Li, and Qihua Ran (2023). “From rainfall to runoff: The role of soil moisture in a mountainous catchment”. In: *Journal of Hydrology* 625, p. 130060. ISSN: 0022-1694. DOI: https://doi.org/10.1016/j.jhydrol.2023.130060. URL: https://www.sciencedirect.com/science/article/pii/S0022169423010028.

Yusuf, Kamorudeen O., Rasheed O. Obalowu, Gideon T. Akinleye, and Selia I. Adio-Yusuf (Sept. 2020). “Determination of Sorptivity, Infiltration Rate and Hydraulic Conductivity of Loamy Sand using Tension Infiltrometer and Double-Ring Infiltrometer”. In: *FUOYE Journal of Engineering and Technology (FUOYEJET)* 5.2. Open access under CC BY-NC license: https://creativecommons.org/licenses/by-nc/4.0/, pp. 1–. ISSN: 2579-0625. DOI: 10.46792/fuoyejet.v5i2.501. URL: https://engineering.fuoye.edu.ng/journal.

Zalokar, Luka, Maja Kobold, and Mojca Šraj (2021). “Investigation of Spatial and Temporal Variability of Hydrological Drought in Slovenia Using the Standardised Streamflow Index (SSI)”. In: *Water* 13.22, p. 3197. DOI: 10.3390/w13223197.

Zhang, Keying, Zhansheng Ji, Xiaoliang Luo, Zhenyi Liu, and Hua Zhong (2024). “Flood Simulation in the Complex River Basin Affected by Hydraulic Structures Using a Coupled Hydrological and Hydrodynamic Model”. In: *Water* 16.17. ISSN: 2073-4441. DOI: 10.3390/w16172383. URL: https://www.mdpi.com/2073-4441/16/17/2383.

A

Python code

The code used in this thesis can be found in an online repository on GitHub:

`https://github.com/adelsolarschaa/Thesis-Droogteanalyse`

B

DinoLoket cross-section

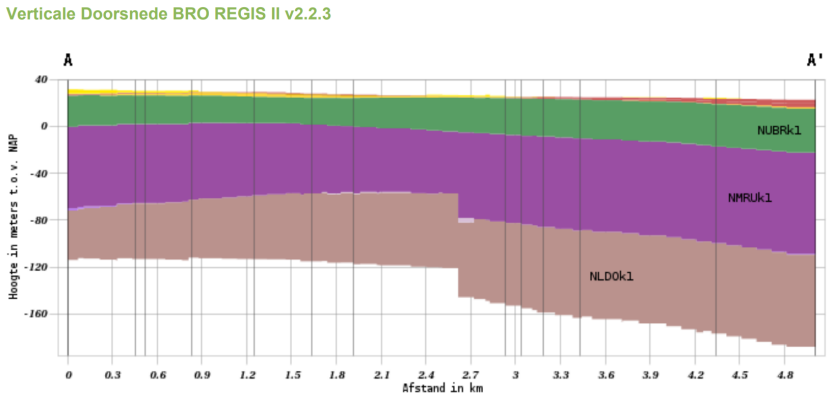

Figure B.1: Cross-section illustrating vertical depth of layers along length of brook, created by tracing a line along the brook and retrieved from TNO – Geological Survey of the Netherlands (n.d.[c]).

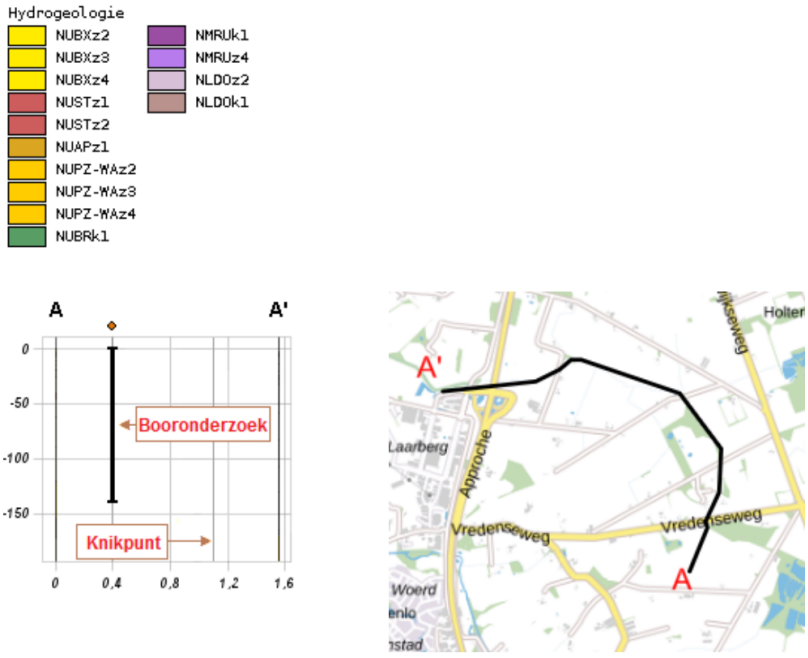

Figure B.2: Specification of cross-section with REGIS II hydrogeological unit codes, retrieved from TNO – Geological Survey of the Netherlands (n.d.[c]).

C

Correlation analysis drought events

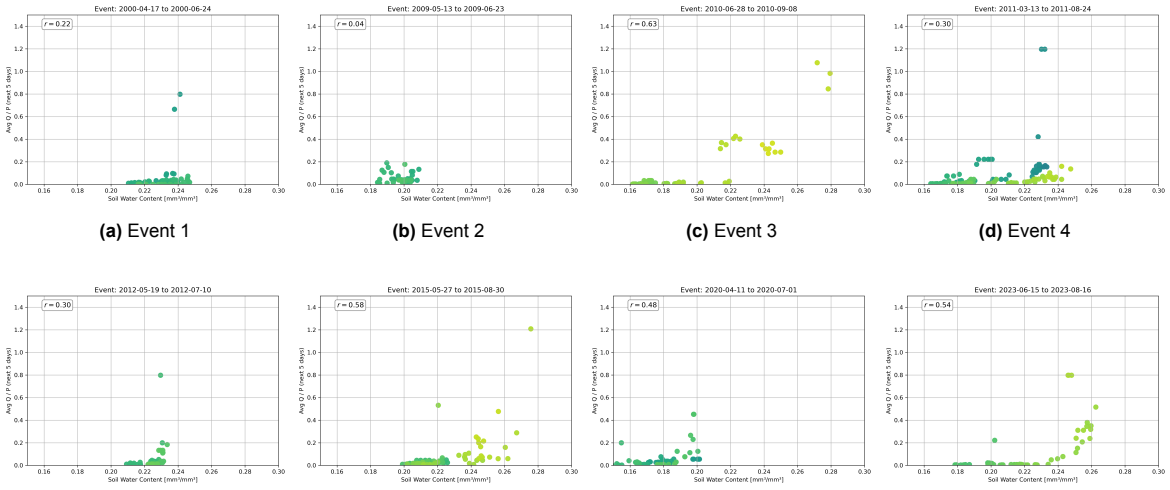

(a) Event 1 **(b)** Event 2 **(c)** Event 3 **(d)** Event 4

(e) Event 5 **(f)** Event 6 **(g)** Event 7 **(h)** Event 8

Figure C.1: Overview of twelve summer drought events followed by peak flow.

D

Correlation analysis drought events

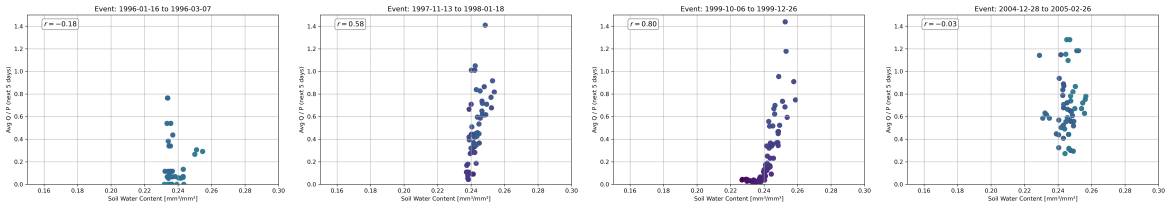

(a) Event 1 **(b)** Event 2 **(c)** Event 3 **(d)** Event 4

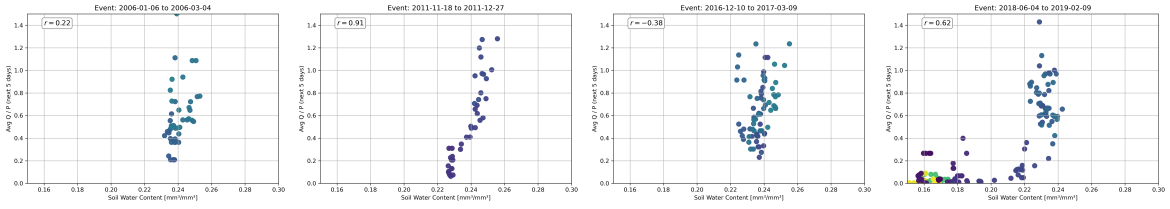

(e) Event 5 **(f)** Event 6 **(g)** Event 7 **(h)** Event 8

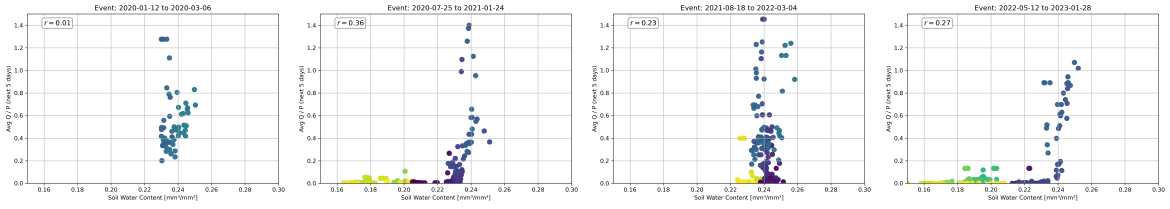

(i) Event 9 **(j)** Event 10 **(k)** Event 11 **(l)** Event 12

Figure D.1: Overview of twelve winter drought events followed by peak flow.

E

Drought - peak flow events

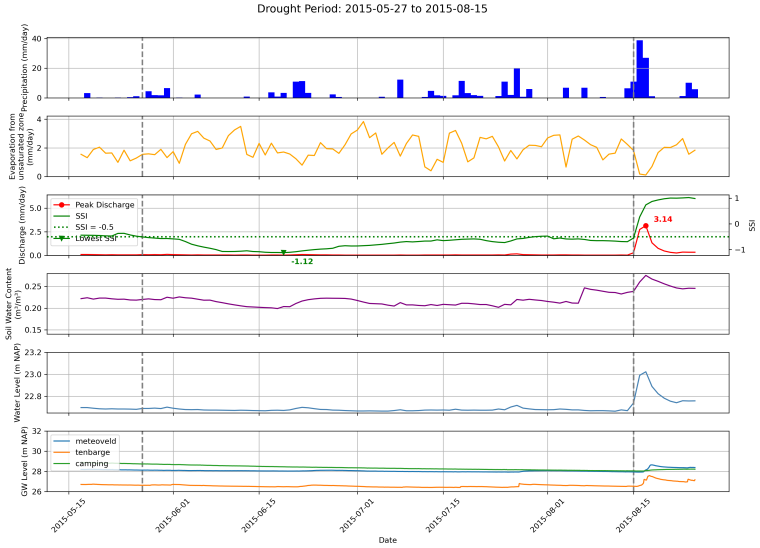

Figure E.1: Drought period 1: validation event.

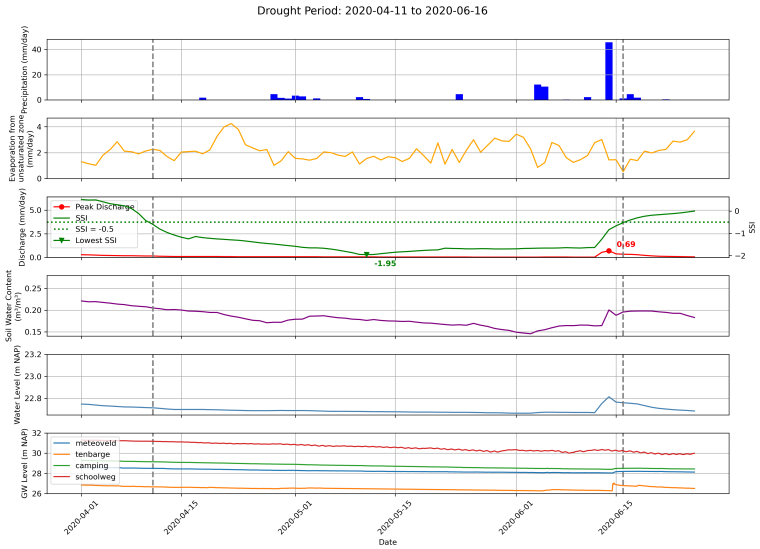

Figure E.2: Drought period 2: validation event.

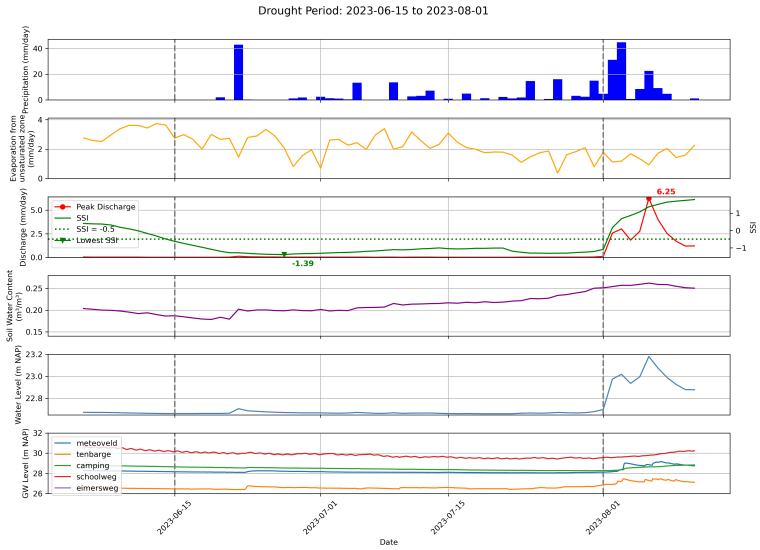

Figure E.3: Drought period 3: calibration event.

F

Input 2015 validation event

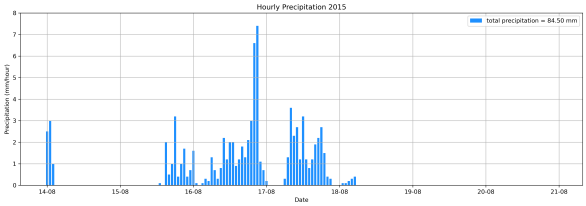

(a) P

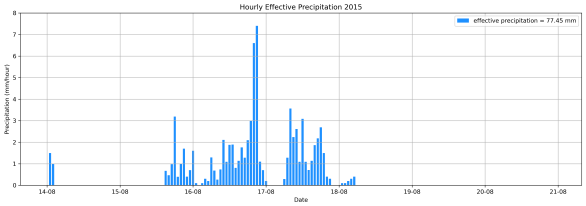

(b) P_E

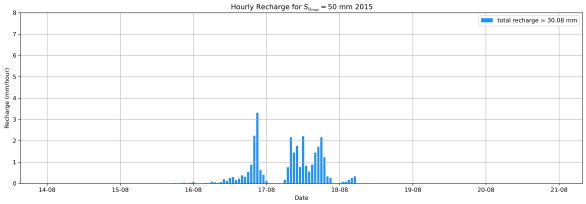

(c) R with $S_{U,\max}$ = 50 mm

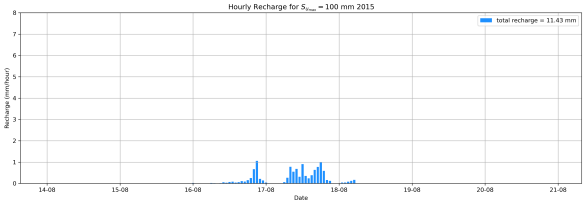

(d) R with $S_{U,\max}$ = 100 mm

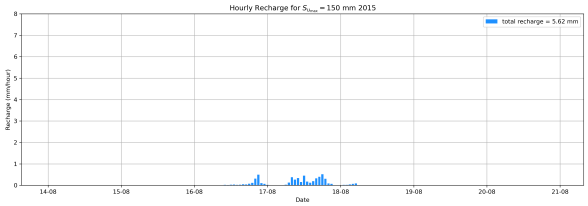

(e) R with $S_{U,\max}$ = 150 mm

Figure F.1: Hydrological input variables for 2015 event.

G

Input 2020 validation event

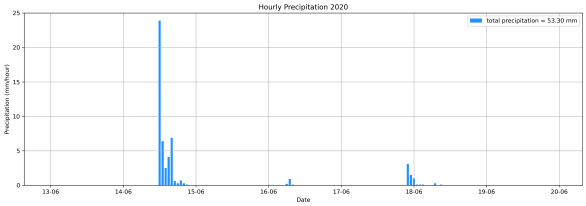

(a) P

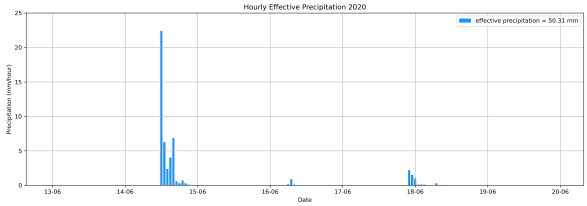

(b) P_E

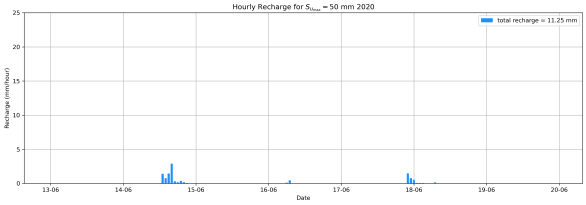

(c) R with $S_{U,\max}$ = 50 mm

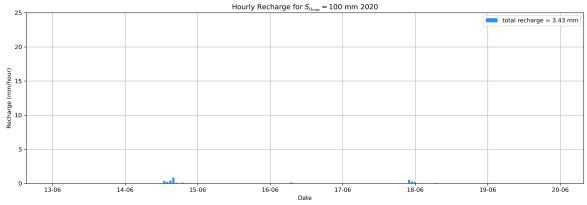

(d) R with $S_{U,\max}$ = 100 mm

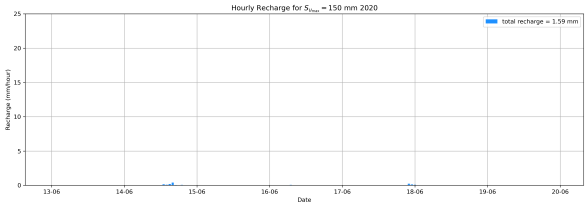

(e) R with $S_{U,\max}$ = 150 mm

Figure G.1: Hydrological input variables for 2020 event.

H

Input 2023 calibration event

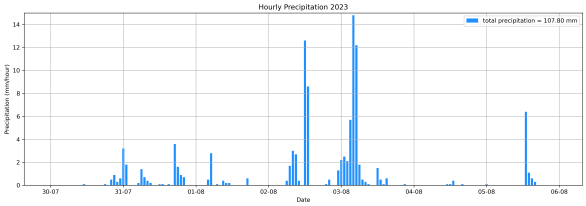

(a) P

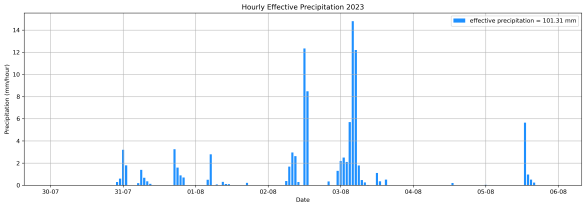

(b) P_E

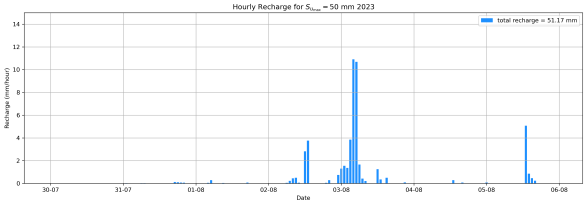

(c) R with $S_{U,\max}$ = 50 mm

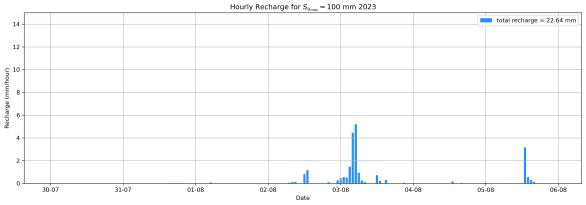

(d) R with $S_{U,\max}$ = 100 mm

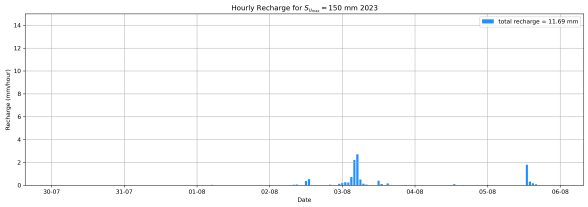

(e) R with $S_{U,\max}$ = 150 mm

Figure H.1: Hydrological input variables for 2023 event.

I

Horton infiltration calibration

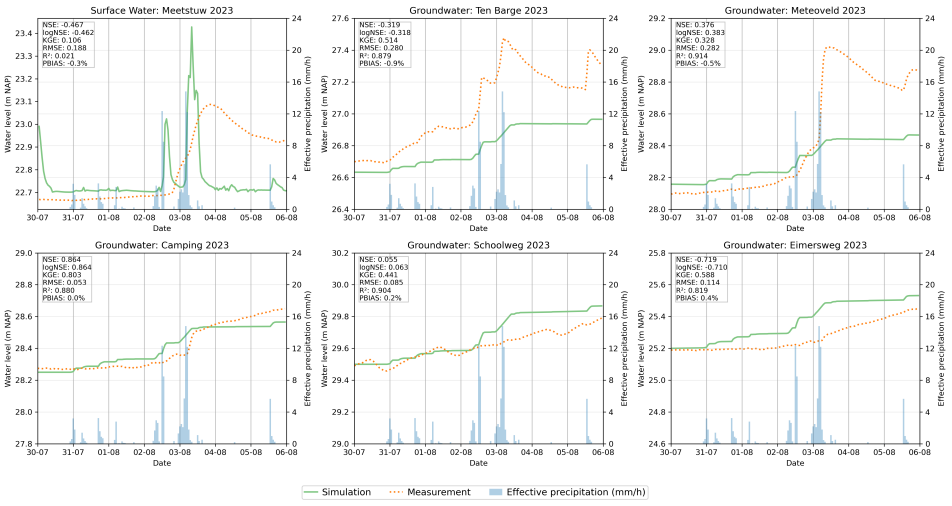

(a) Groundwater and surface water results

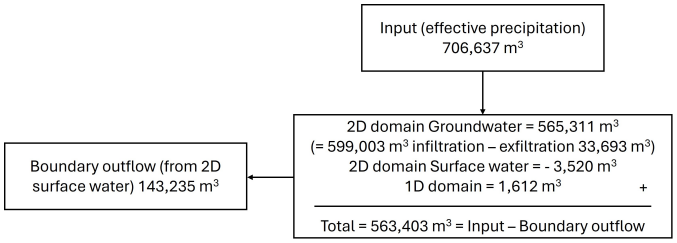

(b) Water balance schematic

Figure I.1: Horton clay: groundwater and surface water results (top) and corresponding water balance schematic (bottom). Fluxes in water balance schematic are given in m^3 over the one-week simulation period.

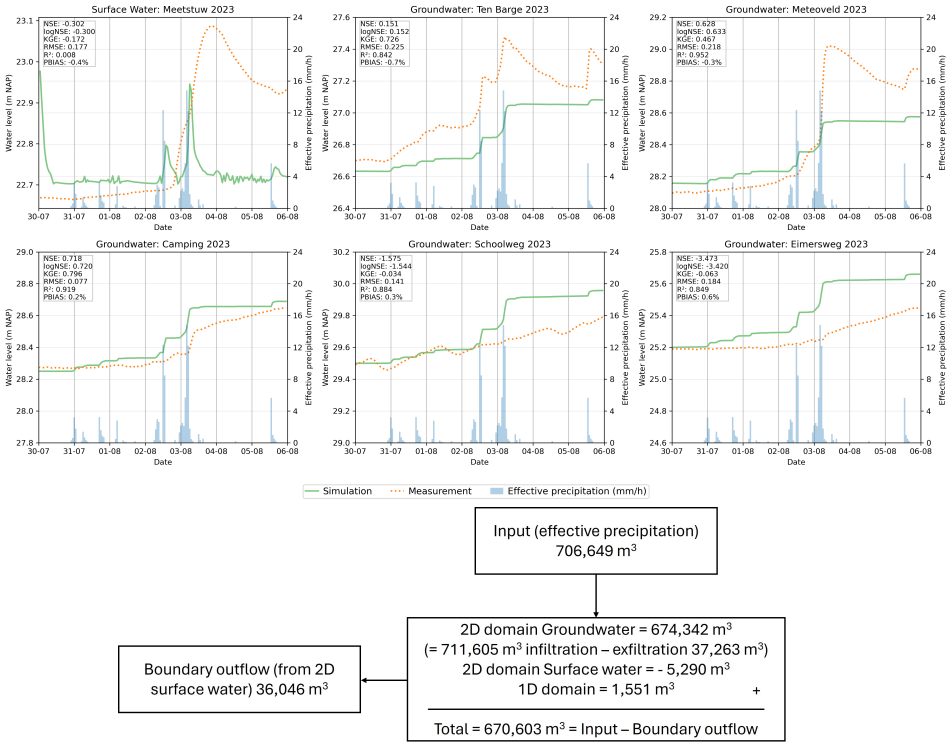

(a) Horton infiltration between clay and loamy sand: results (top) and water balance schematic (bottom). Fluxes in water balance schematic are given in m^3 over the one-week simulation period.

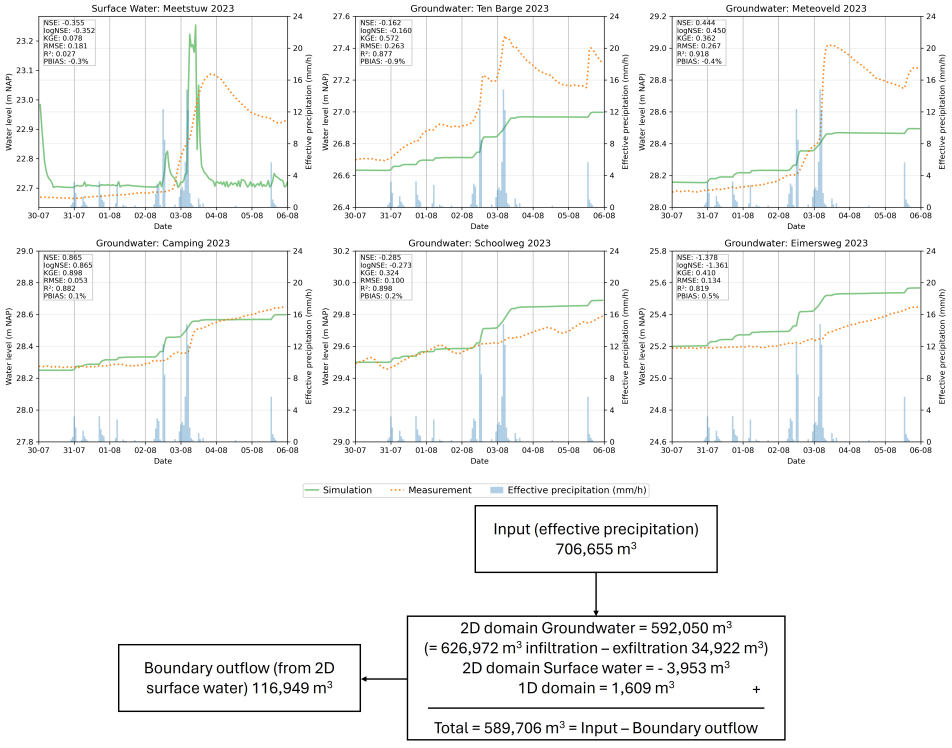

(b) Horton infiltration between clay and values for Figure I.2a: results (top) and water balance schematic (bottom). Fluxes in water balance schematic are given in m^3 over the one-week simulation period.

Figure I.2: Horton infiltration calibration: Cal1 (top) and Cal2 (bottom).

J

Effective porosity calibration

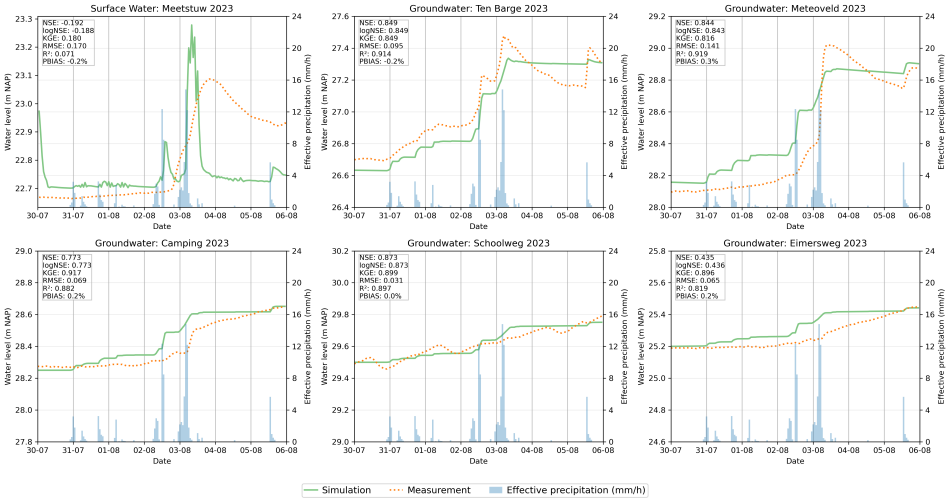

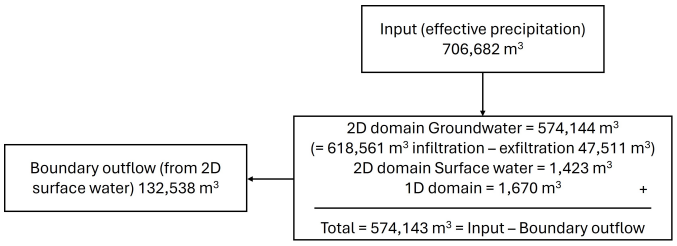

Figure J.1: Results with final effective porosity raster (top) and corresponding water balance schematic (bottom). Fluxes in water balance schematic are given in m^3 over the one-week simulation period.

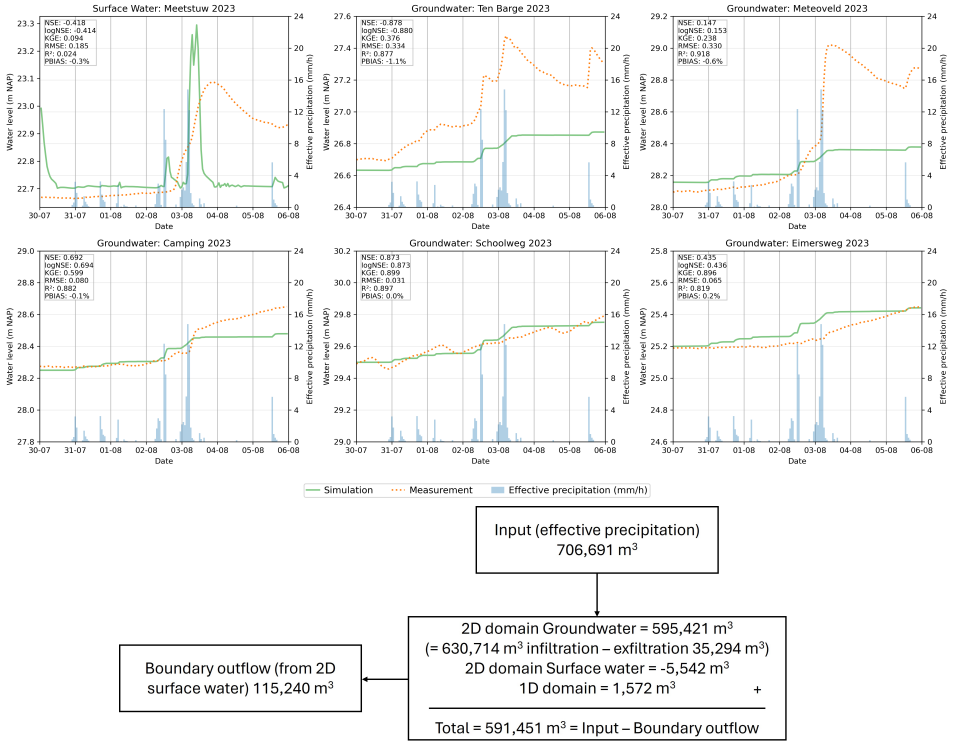

Figure J.2: Results with uniform effective porosity of 0.35 (top) and corresponding water balance schematic (bottom). Fluxes in water balance schematic are given in m^3 over the one-week simulation period.

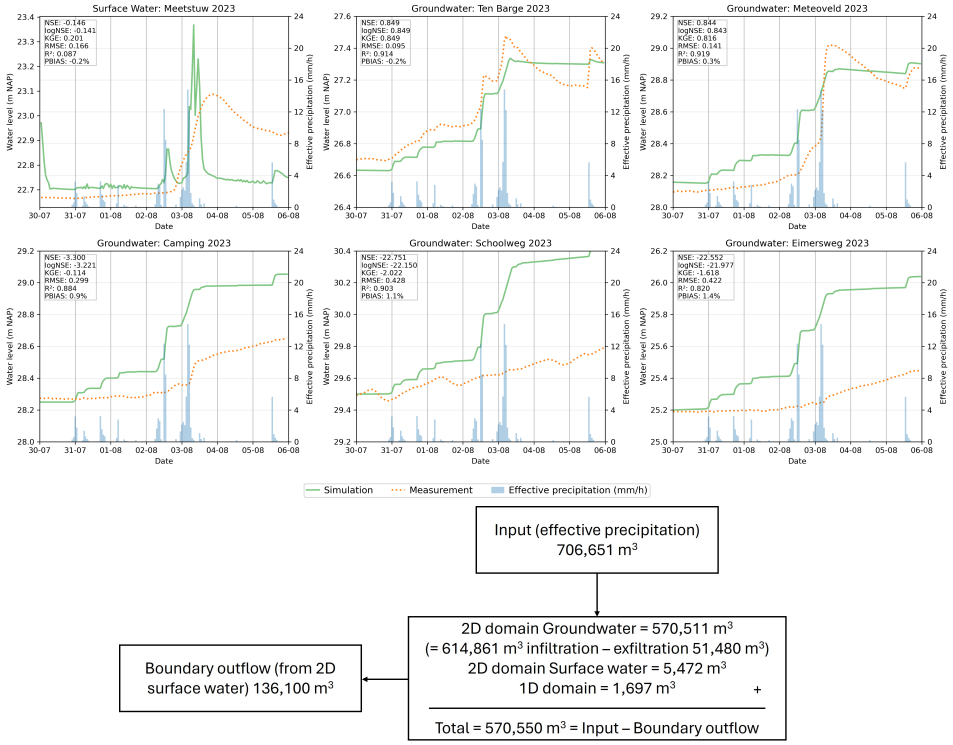

Figure J.3: Results with uniform effective porosity of 0.1 (top) and corresponding water balance schematic (bottom). Fluxes in water balance schematic are given in m^3 over the one-week simulation period.

K

Hydraulic conductivity calibration

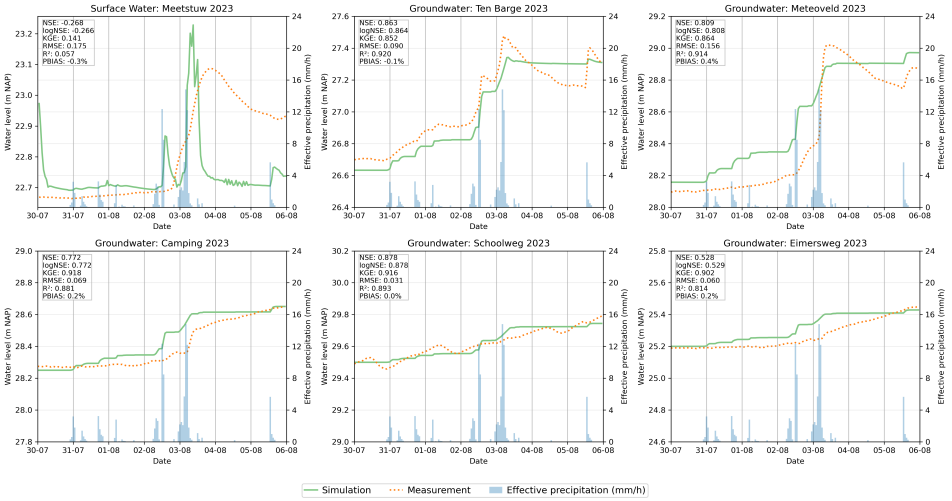

Figure K.1: Hydraulic conductivity low: groundwater and surface water results (top) and corresponding water balance schematic (bottom). Fluxes in water balance schematic are given in m^3 over the one-week simulation period.

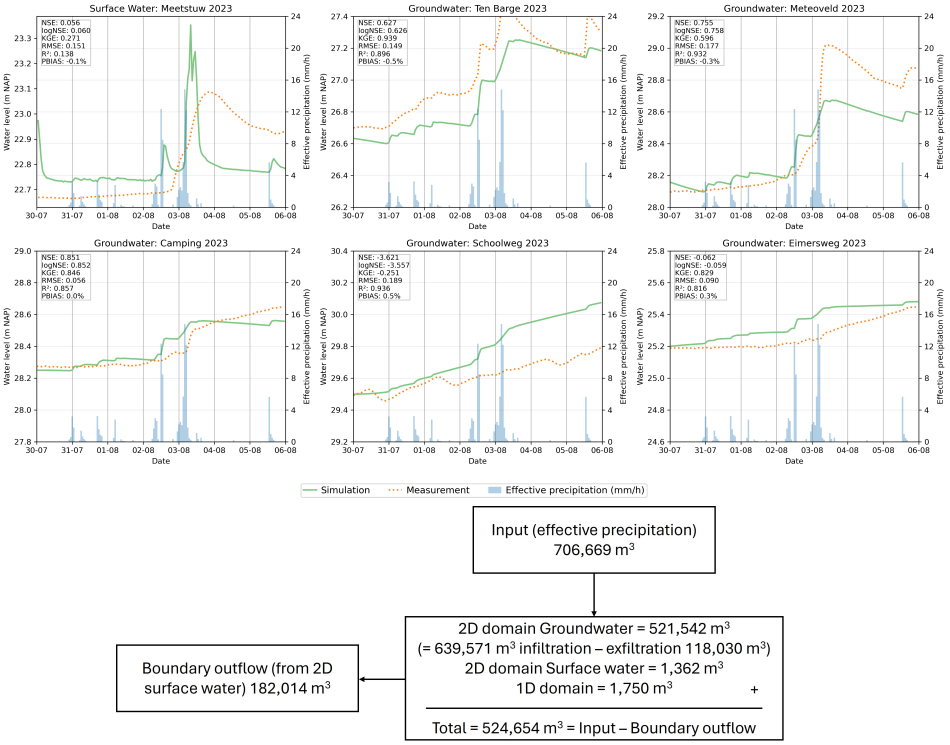

Figure K.2: Hydraulic conductivity high: groundwater and surface water results (top) and corresponding water balance schematic (bottom). Fluxes in water balance schematic are given in m^3 over the one-week simulation period.

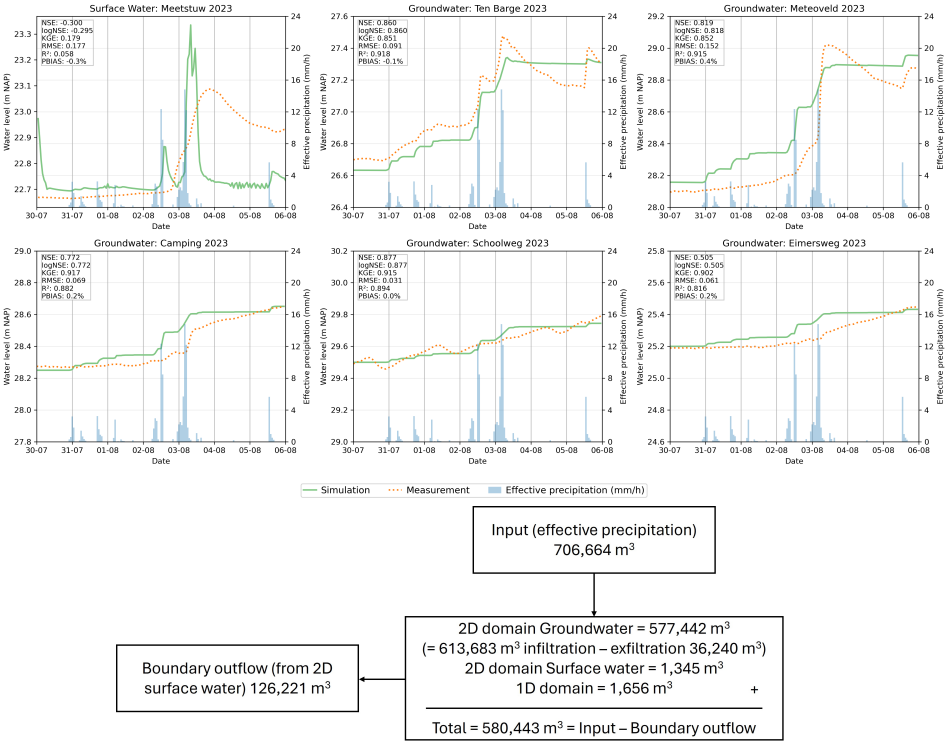

Figure K.3: Hydraulic conductivity calibrated: groundwater and surface water results (top) and corresponding water balance schematic (bottom). Fluxes in water balance schematic are given in m^3 over the one-week simulation period.